LUND UNIVERSITY
Faculty of Science

Development and characterization of tissue-mimicking phantom materials for photoacoustic imaging

Chen Xu

Thesis submitted for the degree of Master of Science
Project duration: 10 months

Supervised by Nina Reistad and Magnus Cinthio / Sune Svanberg

Department of Physics
Division of Atomic Physics
May 2019

LUND UNIVERSITY

Development and characterization of tissue-mimicking phantom materials for photoacoustic imaging

Author:
Chen Xu

Supervisors:
Nina Reistad
Magnus Cinthio
Sune Svanberg

LUND
UNIVERSITY

A thesis submitted in fulfillment of the requirements for the degree of Master of science

Division of Atomic Physics
Department of Physics

Lund Spring 2019

Abstract

Tissue-mimicking phantoms are of great interest in the development of bio-medical applications. Instead of applying to biological tissues directly, phantoms enable stable and easy accessibility to validate spectroscopy systems and measuring processes. This thesis project is centered on the development and characterization of phantoms.

The interaction between light and biological tissue is mainly characterized by the absorption and scattering coefficients. The propagation of light inside tissue can be described by the diffusion theory and Monte Carlo (MC) simulations. Spectroscopy methods such as the collimated transmission spectroscopy (CTS) and the photon time of flight spectroscopy (pToFs) were used to measure the optical properties of the phantoms.

Previous research on phantom materials will be summarized. In particular, the styrene-ethylene/butylene-styrene (SEBS) copolymer was studied and used to produce oil-based phantoms for photoacoustic imaging (PAI). By adding oil-based colored ink and TiO_2 to the gel mixture made with SEBS powder and paraffin oil, oil-based SEBS phantoms with tunable absorption and scattering coefficients were manufactured. Together with good time stability and easy reproducibility, test results from PAI showed that these SEBS phantoms were able to provide good image quality and depth resolution within the near infrared wavelength range.

List of abbreviations

AOTF	Acoustic optical tunable filter
APD	Avalanche photodiode
BPC	Black plastic color
CFD	Constant fraction discriminators
ICG	Indocyanine green
LDPE	Low-density polyethylene
LG	Light green
MB	Methylene blue
MC	Monte Carlo
MCA	Multi-channel analyzer
NIR	Near infrared
PAI	Photoacoustic imaging
PB	Prussian blue
PC	Personal computer
pToFS	Photon time of flight spectroscopy
PVA	Polyvinyl alcohol
PVCP	Polyvinyl chloride plastisol
RF	Radio frequency
RM	Rubine magenta
RTE	Radiative transfer equation
SDS	Source-detector separation
SEBS	Styrene-ethylene/butylene-styrene
TAC	Time to amplitude converter
VIS	Visible
VOA	Variable optical attenuator

Contents

Chapter 1

Introduction

Phantoms are artificial objects that are designed to be used in biological imaging systems. The development of new bio-medical imaging systems motivates the use of phantoms with specific properties. Functioning as significant tools to standardize systematic operations, characterize data measurements and provide imaging quality control in practical use [1], phantoms play an important part in inter-system and inter-lab comparisons. Among them, phantoms mimicking the optical and acoustic properties of biological tissues are of great importance. Instead of using real biological tissues, preliminary measurements with phantoms are useful in system testing and accurate calibration [2]. Tissue-mimicking phantoms should have similar absorption coefficient (μ_a) and scattering coefficient (μ_s) or reduced scattering coefficient (μ_s') as tissues, which are the two main parameters that characterize the optical properties. In particular, phantoms used for photoacoustic imaging (PAI) should also present acoustic properties similar to those for tissues, such as the speed of sound (v) inside and the acoustic attenuation (α). The study of phantoms with stable optical and acoustic properties and good time durability has been carried out for several decades. However, the characterization of phantom materials and recipes for standardized phantoms are still in great need [3].

In this thesis project, materials for tissue-mimicking phantoms are summarized and studied. Particular absorbers and scatterers were characterized using spectroscopy methods. The collimated transmission spectroscopy (CTS) system was used to measure the extinction of the samples through a wide wavelength range. The time-resolved photon time of flight spectroscopy (pToFS) system was adopted to measure the optical properties by analyzing the time-broadened pulses and extracting the information of μ_a and μ_s'. Recipes for producing oil-based solid phantoms were developed. Methods of tuning the optical properties of these phantoms within the near infrared region were discussed and validated. Advanced oil-based solid phantoms were produced and tested by the photoacoustic imaging (PAI) system at the Department of Ophthalmology, Clinical Sciences Lund, Lund University. The performance of these advanced phantoms and the ability of the PAI system to detect complex geometry and distinguish different absorbers was evaluated by analyzing the photoacoustic images.

In summary, this thesis project is aimed at demonstrating the value of tissue-mimicking phantoms. Materials for such phantoms were summarized and characterization of certain materials were performed. The manufacturing protocols and recipes of both liquid and solid phantoms were developed. The PAI system was tested and the acquired photoacoustic images were analyzed. The future applications of phantoms in medical imaging and pre-clinical diagnosis were also studied.

Chapter 2

Theory

2.1 Light propagation in tissue

Biological tissues are usually simplified as turbid media where incident light experiences multiple processes. The reflection, refraction, absorption and scattering processes in a biological medium where both absorbers and scatterers [4] exist are shown in Figure 2.1.

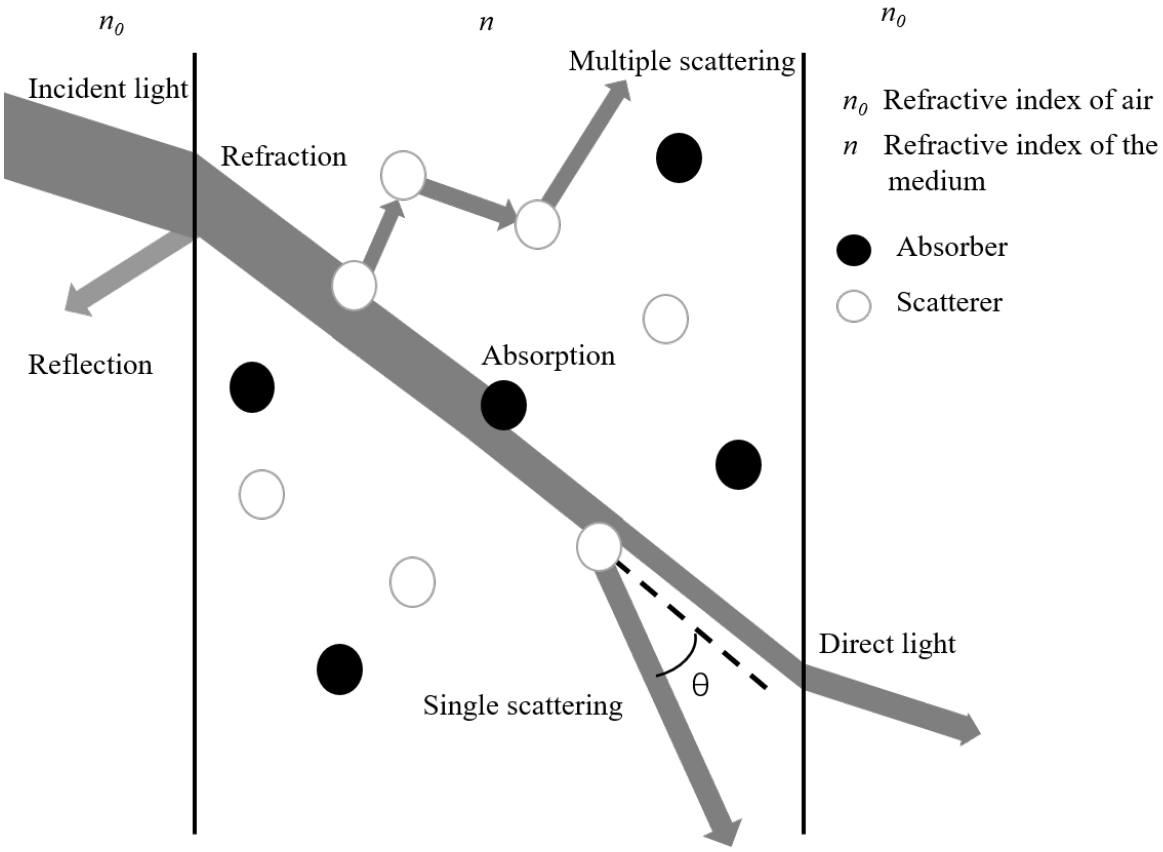

Figure 2.1: Reflection, refraction, absorption and scattering processes in a biological medium with refractive index n.

Reflection and refraction would happen on the boundary when the medium is illuminated. The light propagating inside the medium will experience absorption and scattering processes. These two processes are characterized by the absorption coefficient (μ_a) and scattering coefficient (μ_s). The reflection, absorption and scattering

processes give a lot of information of the biological tissue. Various kinds of tissue spectroscopy methods are established basing on detecting these phenomena. Hence, it is of great important to understand the interaction between light and biological tissues.

2.1.1 Scattering

Scattering happens when particles interacting with the incident photons and usually the direction of propagating light will be changed. The scattering coefficient (μ_s) defined as the probability of a incident photon to be scattered per unit length is used to describe this process. A scattering process is defined as elastic scattering if it observes the conservation of energy. Otherwise it is defined as inelastic scattering. Inelastic scattering such as Raman scattering can be used to determine the chemical component of the scatterers by extracting energy information from the scattered light. In biological tissue, the scattering process is usually simplified as elastic scattering in which no energy information is contained. Elastic scattering can also be divided into two categories depending on the size of the scattering particles. Rayleigh scattering refers to the case where the size of the particles are small compared with the wavelength of the interacting light. And Mie scattering is applied when the size of scattering particles are similar or larger than the wavelength of the interacting light. For Rayleigh scattering, this process is strongly wavelength dependent and mostly isotropic. The blue sky can be explained by Rayleigh scattering. However, in biological tissue where the size of cells and particles are usually more than several micrometers, the scattering is no longer isotropic and Mie scattering theory is applied.

The direction of the out-coming light in scattering process is decided by the anisotropy factor (g) and the phase function ($p(\theta)$). As defined in Figure 2.1, the incident light is scattered to a new direction which makes an angle θ to original direction. The anisotropy factor g is the average of the cosine of θ:

$$g = < \cos(\theta) > \tag{2.1}$$

The g factor equals to 0 in isotropic scattering where scattering happens in all directions. When the g factor equals to 1, it means all the scattering happens in forward direction. On the contrary, when the g factor equals to -1, it means all the scattering happens in backward direction. Usually g factor varies from -1 to 1. The phase function describes the probability that the incident light is scattered to a new direction with a angle θ to the original direction given by the Henyey-Greenstein phase function [5]:

$$p(\theta) = \frac{1}{4\pi} \frac{1 - g^2}{(1 + g^2 - 2 \cdot g \cdot \cos(\theta))^{3/2}} \tag{2.2}$$

Figure 2.2 below is obtained from the online Monte Carlo (MC) simulation program, the Multi-scattering software [6]. In this figure, the scattering phase function at chosen parameters of a wavelength at 700 nm, particle size 0.2 μm and exponential size distribution was calculated and the resulting g factor equalled to 0.7.

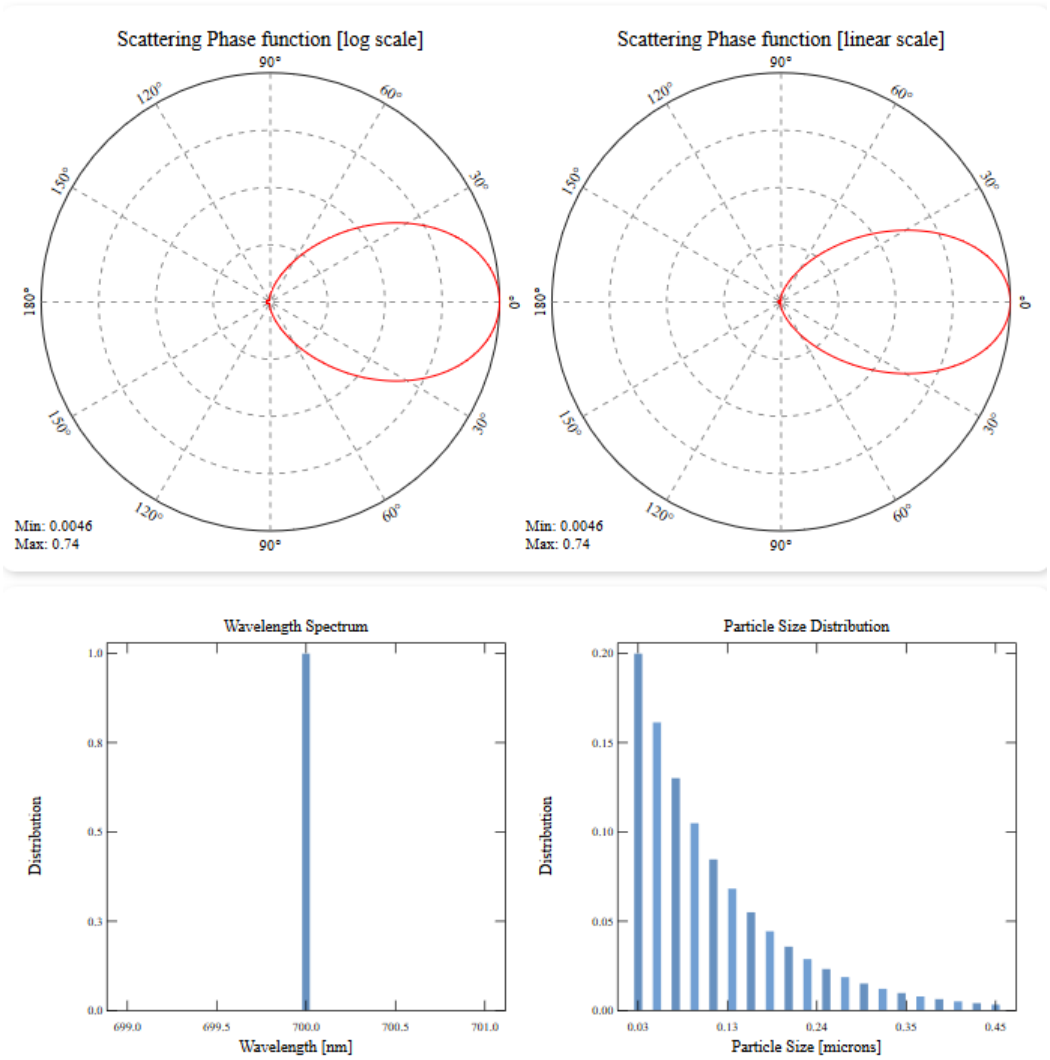

Figure 2.2: Images generated by Multi-scattering software. Top left: scattering phase function $p(\theta)$ in log scale; Top right: scattering phase function $p(\theta)$ in linear scale; Bottom left: wavelength spectrum distribution; Bottom right: particle size distribution.

For multiple scattering processes, the reduced scattering coefficient (μ_s') is introduced to describe the light scattered to a new direction:

$$\mu_s' = \mu_s(1-g) \tag{2.3}$$

μ_s' equals to 0 when the g factor equals to 1, which means that all the light would pass the medium without being scattered.

2.1.2 Absorption

Biological tissue usually consists of different components with various energy band structures. Incident photons that match the transition condition between energy bands will be absorbed. The absorbed energy is transformed to heat, re-emitting

photons or other form of energy. The absorption process is described by the Beer-Lambert law.

$$I = I_0 e^{-\mu_a \cdot L} \tag{2.4}$$

where I is the intensity of transmitted light, I_0 is the intensity of incident light, μ_a is the absorption coefficient and L is the path length inside the absorbing medium.

The absorption spectrum of human tissue is characterized by several main components such as water and blood. For example, the absorption spectrum of oxygenated blood is mainly characterized by the oxygenated hemoglobin in blood cells, while for de-oxygenated blood, de-oxygenated hemoglobin is the dominating absorber. The absorption of blood falls off at around 650 nm and the absorption of water starts at approximately 1300 nm so that many medical applications are carried out within this wavelength range. This region is named as the tissue optical window.

2.2 Mathematical models

The absorption coefficient (μ_a) and scattering coefficient (μ_s) characterize the optical properties of the medium. These two parameters are used in mathematical models describing the light propagation inside the medium.

2.2.1 Radiative transfer equation

The radiative transfer equation (RTE), based on the law of conservation of energy, describes how light propagates through the medium [7]. Different processes are taken into consideration to calculate the radiance change inside a small volume element $d\Omega$. The equation is expressed as:

$$\frac{1}{c}\frac{dL(\vec{r},\hat{s},t)}{dt} = -\mu_t L(\vec{r},\hat{s},t) \pm \nabla[L(\vec{r},\hat{s},t)\cdot\hat{s}] + \mu_s \int_{4\pi} \Phi(\hat{s},\hat{s}')L(\vec{r},\hat{s},t)d\Omega' \tag{2.5}$$

where $L(\vec{r},\hat{s},t)$ is the radiance as a function of position ($\vec{r}$), incident direction ($\hat{s}$) and time (t), c is the speed of light, $\mu_t = \mu_a + \mu_s$ is the extinction coefficient, $\Phi(\hat{s},\hat{s}')$ is the fluence rate from ($\hat{s}$) to ($\hat{s}'$)). The term to the left of the equation refers to the rate of change in radiant power inside this small volume element $d\Omega$. Terms to the right refer to extinction (absorption and scattering out of the volume), external divergence or convergence, radiant power scattered from other volume element and redirected to $\hat{s}'$, respectively.

2.2.2 Diffusion equation

If the radiance $L(\vec{r},\hat{s},t)$ is not strongly dependent on direction, the RTE with complicated form can be simplified by using the fluence rate $\Phi(\vec{r},t)$ to replace the radiance $L(\vec{r},\hat{s},t)$. The fluence rate $\Phi(\vec{r},t)$ is then just the integral of radiance over all solid angles. Expanding the function of radiance into spherical harmonics and assuming that the temporal variation of current density is small, the diffusion equation after the

simplification of the RTE can be written as [8]:

$$\frac{1}{c}\frac{\partial\Phi(\vec{r},t)}{\partial t} - D\nabla^2\Phi(\vec{r},t) + \mu_a\Phi(\vec{r},t) = 0 \tag{2.6}$$

where $D = \frac{1}{3(\mu_a+\mu_s')}$ is the diffusion coefficient, $S(\vec{r},t)$ describes the light sources.

2.2.3 Analytical solutions

The diffusion equation is valid when scattering is sufficiently higher than absorption ($\mu_s \gg \mu_a$) and only applies to simple geometries such as infinite, semi-infinite and slab medium. Analytical solutions to the diffusion equation are discussed here.

Infinite medium

The simplest case is the analytical solution when light is incident into an infinite extended homogeneous medium by a point source. The solution can be written as [9]:

$$\Phi(\vec{r},t) = \frac{c}{(4\pi Dct)^{3/2}} \cdot e^{-\mu_a ct} \cdot e^{-\frac{r^2}{4Dct}} \tag{2.7}$$

Semi-infinite medium

Considering the case for a semi-infinite medium, it is assumed that the light source and the detector are both placed at the surface. This is more realistic and most experimental setups are built under this circumstance. The fundamental detecting diagram for the pToFS system used in this thesis project is shown in Figure 2.3.

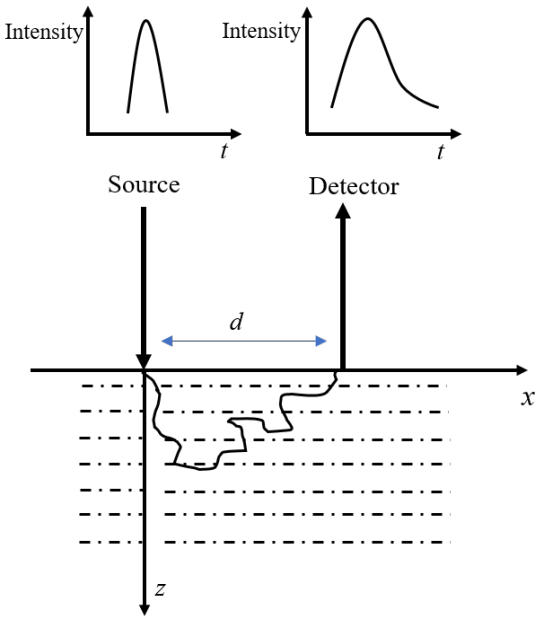

Figure 2.3: Diagram of detection. Top left: time profile of the incident pulse; Top right: time profile of the detected broadened pulse; Bottom: schematic picture of the detecting model for semi-infinite medium.

In this case, the incident light is provided by an optical fiber and the detecting fiber is placed at a distance (d) from the light source. The size of the source fiber and the detector fiber are neglected and all the light is assumed to be scattered at the transport mean free path depth (z_0) [8], with

$$z_0 = \frac{1}{\mu_a + \mu_s'} \tag{2.8}$$

The internal reflectance (r_d), due to the mismatch of refractive index (n) between the air and the tissue [10], is defined as

$$r_d = -1.440 n_{rel}^{-2} + 0.710 n_{rel}^{-1} + 0.0668 + 0.0636 n_{rel} \tag{2.9}$$

where n_{rel} is the ratio between the refractive index of the tissue and the air, $n_{rel} = n_{tissue}/n_{air}$.

Different boundary conditions give different expression of the fluence rate $\Phi(\vec{r}, t)$ when solving the diffusion equation. The extrapolated boundary condition makes a compromise between precision and simplification and has been proved to provide a good fit with real results. Under the extrapolated boundary condition, the fluence rate $\Phi(\vec{r}, t)$ is assumed to be zero not at the physical boundary of the medium but an extrapolated boundary at a distance z_e to the real boundary [10], with

$$z_e = 2D\frac{1 + r_d}{1 - r_d} \tag{2.10}$$

And by invoking the principle of a negative image source of the real source located at z_p,

$$z_p = z_0 + 2z_e \tag{2.11}$$

the time dependent fluence rate $\Phi(\vec{r}, t)$ can be written as the sum of the two sources in an infinite medium as [10, 11]

$$\Phi(\vec{r}, z, t) = \frac{c}{(4\pi Dct)^{3/2}} \cdot e^{-\mu_a ct} \cdot [e^{-\frac{(z-z_0)^2+r^2}{4Dct}} - e^{-\frac{(z+z_p)^2+r^2}{4Dct}}] \tag{2.12}$$

In real measurements, the diffuse reflectance (R) defined as the number of photon reaching the detector per unit area per unit time is measured. R is derived from the Fick's law [12].

$$R = |-D\nabla\Phi(\vec{r}, z, t)|_{z=0} \tag{2.13}$$

Applying Eq 2.12 into Eq 2.13, the diffuse reflectance R at the distance d can be written as [9, 11]

$$R(d, t) = \frac{1}{2}(4\pi Dct)^{-3/2} t^{-5/2} e^{-\mu_a ct} \cdot [z_0 e^{-\frac{z_0^2+d^2}{4Dct}} + z_p e^{-\frac{z_p^2+d^2}{4Dct}}] \tag{2.14}$$

2.2.4 Monte Carlo simulation

When dealing with media in which both absorption and scattering are strong, for example, in biological tissues, the MC simulation method is used to give a numerical solution of RTE. Based on the random walk method, the MC simulation utilizes

multiple calculations of a large number photons to study their behaviour and simulate the propagation of light inside the medium, with both scattering and absorption taken into consideration. The whole process can be described as given below.

The medium being studied is divided into small elements and virtual particles without any wave characteristic are used to simulate the incident photons. Each particle will experience a loop process. A path length factor based on a random function representing the probability of surviving is introduced. The initialized particle is moved following this factor. Then it is judged to be absorbed or not. If not absorbed, it is considered to be scattered into a new direction which follow Eq 2.2. This particle will be moved and assessed again until it is decided to be absorbed. After that, a new particle is again initialized and introduced into the loop and the procedure runs again. By repeating the whole loop process on a huge number of photons, the MC simulation can describe the propagation of light inside the medium accurately. The geometry structure is also important in the model and different boundary conditions result in different outputs [13].

2.3 Phantom materials

There are a lot of materials that have been proposed for optical and ultrasound imaging phantoms. By changing the concentration of absorbers, scatterers and the recipe for the base material, the optical and acoustic properties of the phantoms can be varied as in biological tissues. In principle, phantoms can be divided into liquid and solid phantoms. For liquid phantoms and water-based solid phantoms, water-based materials are used as the base material so that water soluble absorbers and scatterers are adopted. However, hydrophilic solvent are not applicable for oil-based solid phantoms. A review of literature of absorbers, scatterers and different base material for tissue-mimicking phantoms follows.

2.3.1 Liquid phantoms

In this thesis project, liquid phantoms made by adding absorber and scatterer in water were used to validate the spectroscopy methods. Liquid phantoms are widely used because they are easy and inexpensive to produce. Meanwhile, it is usually very convenient to control their optical properties by changing the concentrations of absorbers and scatterers. Water-based materials such as gelatin, agar and polyvinyl alcohol are also used to produce phantoms. The disadvantages of these water-based phantoms are easy degradation by microbial invasion and dehydration, which limits the temporal stability [2].

Absorbers

Absorbers that can be solved in water are usually used to control absorption properties of phantoms. A simple review of absorbers reported to be used in tissue-mimicking phantom production is shown in Table 2.1.

Table 2.1: Absorbers used in liquid phantoms.

Absorbers	Absorption band	Usage requirements
India ink	Absorption at all wavelength.	Sample base is usually needed for reproducible measurement.
Methylene blue	Peak absorption around 650 nm.	Slight peak shift in liquid solvent.
Indocyanine green	Peak absorption around 790 nm.	Slight peak shift in liquid solvent.
Other molecular dyes	Peak at particular wavelengths	Pre-dissolution needed for some oil-based phantoms.
Synthetic melanin and blood-mimicking fluid	Similar to tissue.	Market products.

India ink of various brands in the market are widely used in water-based phantoms. A thorough study of their absorption properties and reliable reference values were reported [14]. Usually ink-water bases with known concentration was made and measured before using it in phantom production. The usage of Methylene blue (MB) [15], Indocyanine green (ICG) [16] and other molecular dyes are also reported. With strongly wavelength dependent absorption property, these absorbers are usually adopted for single wavelength applications. They can be disolved in water directly, or pre-dissolution is required in some occasions. Synthetic materials are also of interest in recent medical applications [17].

In this thesis project, three different brands of India ink were bought from market and measured in the laboratory. The results were compared with values from a well-acknowledged paper by Ninni [18].

Scatterers

There are various scatterers used in liquid phantoms to tune the scattering coefficient. A simple review of scatterers used in tissue-mimicking phantoms is shown in Table 2.2 [19] .

Table 2.2: Scatterers used in liquid phantoms.

Scatterers	Temporal stability	Refractive index n	Particle size	Usage
Intralipid	Days	1.45	10 to 500 nm; exponential distribution.	Widely used with well-known property.
TiO_2 powder	Permanent	2.4 to 2.9	20 to 70 nm; single size or exponentially distributed as ordered.	Gelatin and resin phantoms.
Microspheres	Permanent	Varies with material	Single size as ordered.	All phantoms; most accurate

Intralipid is a milk-like solution consisting of small droplets of fat used as intravenously administered nutrient in clinical care. It has good biological compatibility

and organic chemical stability but usually needs to be stored in the fridge. The optical properties of Intralipid 10% within the range from 400 nm to 1100 nm has been well-characterized [20]. The index of refraction of Intralipid is 1.45 and the particle size varies from 10 to 500 nm. The size distribution is exponentially weighted to smaller sizes and it is impossible to get a single size distribution. TiO_2 powder is a widely-used matter to provide scattering. Its refractive index ranges from 2.4 to 2.9 and the particle size varies from 20 nm to 70 nm as ordered. Specially ordered polymer microspheres are precise in particle size with almost single size distribution. Small polymer microspheres with size of 20 µm can be made. The refractive index of these microspheres are 1.59.

In this thesis project, Intralipid 20% (Fresenius Kabi AB, Uppsala) was used to provide scattering effects in water-based phantoms. The scattering coefficient for Intralipid 20% in the rage of 400 nm to 900 nm is calculated by Mie theory and provided as [21]:

$$\begin{aligned} \mu_s &= 3.873 \cdot 10^8 \cdot \lambda^{-2.397} / (m\ell/\ell) \\ g(\lambda) &= 1.090 - 6.812 \cdot 10^{-4}\lambda \end{aligned} \tag{2.15}$$

where μ_s is the scattering coefficient and $g(\lambda)$ is the anisotropy factor. The reduced scattering coefficient is

$$\begin{aligned} \mu_s' &= \mu_s(1-g) \\ \mu_s' &= 82.61 - 0.1288 \cdot \lambda + 6.093 \cdot \lambda^2 / m\ell/\ell) \end{aligned} \tag{2.16}$$

2.3.2 Solid phantoms

Solid phantoms usually have better time stability and they are more endurable to environment changes than liquid phantoms. They are also more convenient to be transported around different laboratories. However, it is normally more complex to manufacture solid phantoms since hardening or heating and cooling processes are usually needed. The cost of manufacturing should also be taken into consideration. Errors may be introduced when trying to reproduce known recipes containing small concentrations of absorbers and scatterers.

Recipes of solid phantoms designed for photoacoustic imaging are summarized in Table 2.3.

Solid phantoms can be divided into two categories depending on the base materials: water-based and oil-based solid phantoms. Water-based materials, such as gelatin [22], optical diffuse gel [16] and polyvinyl chloride plastisol (PVCP) [23] are widely used due to their easy accessibility, low cost, and good reproducibility of the human tissue characteristics. However, they still suffer from easy degradation and dehydration. Oil-based materials present good temporal stability since they do not dehydrate from water. The usage of gel wax for photoacoustic imaging was reported [24]. The ability of styrene-ethylene/butylene-styrene (SEBS) copolymer was studied. This copolymer is a structured elastomer with a rigid phase made of styrene structures and a rubber phase made of ethylene–butylene structures [2]. SEBS phantoms were reported to have similar acoustic properties as biological tissues [25] but not any similar optical properties.

Table 2.3: Phantom recipes of solid phantom reported in literature.

Base material	Base property	Absorber	Scatterer
Optically diffusive gel	Water-based	ICG	Intralipid
Gelatin	Water-based	India ink, Direct Red 81, Evans Blue	Intralipid
PVCP	Water-based	Black plastic color (BPC)	TiO_2
Gel wax	Oil-based	Oil-based inks	TiO_2
Polyester resin	Oil-based	Pro-Jet 900NP	TiO_2
SEBS and LDPE	Oil-based		
SEBS and LDPE	Oil-based	Annatto dyes	Glass micro-sphere
SEBS and Glycerol	Oil-based	MB	TiO_2

Tuning optical properties of SEBS phantoms

Study about tuning the optical properties of SEBS phantoms within the wavelength region of interest for the PAI setup used in this project, 680 nm to 970 nm, was carried out.

On the one hand, it is possible to add some other material into the SEBS-oil base gel to change the properties of the whole mixture. For example, combining different concentrations of another copolymer, low-density polyethylene (LDPE), are reported to be able to vary the optical properties [26]. No extra absorbers and scatterers are needed. It was reported that adding LDPE would increase both the absorption and scattering coefficients. Adding glycerol into the SEBS-mineral oil mixture can be another way to adjust the phantoms [15]. Water-based chromophores will then become soluble so Indian ink and other dyes can be added as absorbers, while Intralipid and TiO_2 can be added as scatterers. But then the fabrication procedure becomes more complicated since and unwanted speckles in the photoacoustic images of the SEBS-glycerol phantoms were reported.

On the other hand, seeking for absorbers and scatterers that can be dissolved in mineral oil is more direct to change the optical properties. Early Research has suggested that adding glass microspheres as scatterers and annatto dye dissolved in mineral oil as absorber could be helpful to control the optical properties [27]. This annatto dye absorbs at 532 nm. Different oil-based coloured inks were used in gel-wax, and some color are promising for the wavelength range of interest [24]. Papers related to near-infrared spectroscopy were studied and the usage of molecular absorbers available from the market were reported. The Pro-Jet NP (Fujifilm) absorber series are typical products used as absorber in the near-infrared (NIR) range [28]. Three different products of the series, Pro-Jet 800NP, Pro-Jet 830NP and Pro-Jet 900NP absorb at 775 nm, 810 nm and 865 nm, respectively. These absorbers need to be pre-dissolved in solvent before applying it in phantoms. Meanwhile, these absorbers usually have specific wavelength dependence and careful selection is needed when applying to a PAI system.

Chapter 3

Experimental methods

3.1 Spectroscopy methods

3.1.1 Photon time of flight spectroscopy

The photon time of flight spectroscopy (pToFS) is used to measure optical properties of liquid phantoms. The principal of the system is described as follows. After transmitting a short pulse into a turbid medium, the path length that a photon travels is dependent on the optical properties of the medium. Different path length means different time interval for the photons to arrive at the detector. Consequently, the incident pulse will be broadened and the time profile of the detected pulse can be analyzed to extract the information of absorption coefficient (μ_a) and the reduced scattering coefficient (μ_s') [29]. In pToFS, the diffuse reflectance pulse is collected and a time-correlated single photon counting (TCSPC) card is used for time-resolved measurements. The systematic diagram of the setup is shown in Figure 3.1.

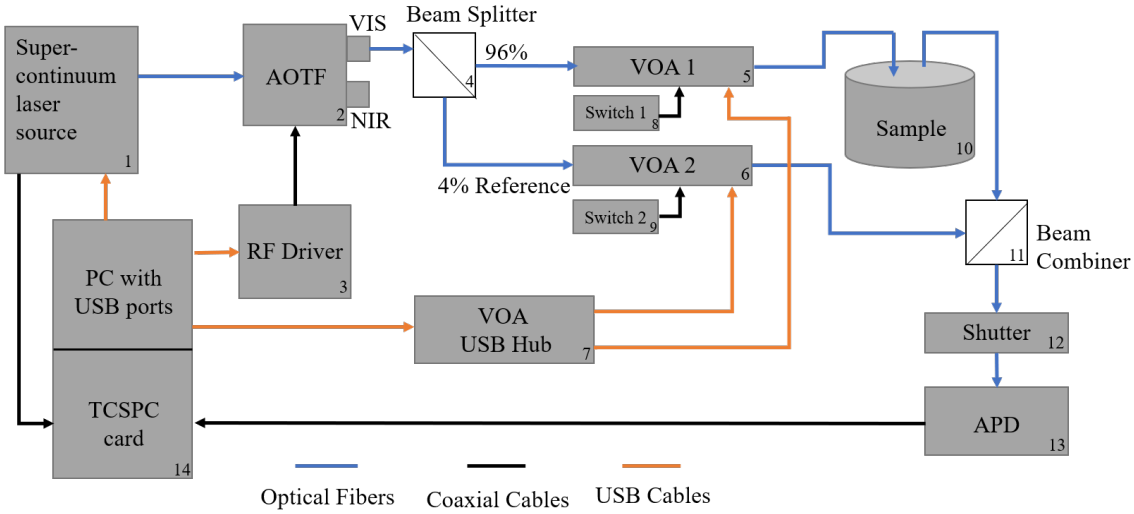

Figure 3.1: Schematic diagram of the pToFS system.

A super-continuum white laser source (Model SC480-10, Fianium, Ltd, Southampton, UK) generates short pulses with pulse duration of 6 picoseconds at a repetition rate of 80 MHz. The output light consists of broadband wavelength from 400 nm to 2100 nm and the maximum power is 10 W. The trigger output of the light source is sent to a computer (PC) as the synchronization clock of the TCSPC card. The

laser source output is sent to an acoustic optical tunable filter (AOTF, Fianium Ltd, Southampton, UK) which has two output ports: Vis (400-700 nm) and NIR 1 (650-1100 nm). These two ports use two different crystals to get a narrow-band filer. The AOTF is driven by a RF (radio frequency) driver and controlled by the program on the PC. Then the narrow band output is sent via a graded-index fiber (core diameter 400 µm, cladding diameter 640 µm, Leoni Fiber Optics, Germany) to a beam splitter, where 4% reflected light is used as a reference and the remaining 96% transmission light is sent to the sample. Two variable optical attenuators (VOA, FVA-3100, OZ Optics Ltd) with an attenuation range from -2.6 dB to -40 dB are applied to control the power of the light incident to the shutter and the detector. The two VOAs are controlled by a USB hub connecting to the PC and can be adjusted by the computer program. A safe light power should be chosen before the light is sent into the sample for performing the measurement. After passing through the sample, the time-broadened pulse is recombined with the time reference pulse by a beam combiner. Then the result is sent through a shutter and finally to a single-photon avalanche photodiode (APD, PD1CTC, Micro Photon Devices). The photodiode is connected to the constant fraction discriminators (CFD) port on TCSPC card on the PC. The synchronization clock signal, triggered by the laser source, is sent to another CFD.

The diagram of the TCSPC-card is shown in Figure 3.2.

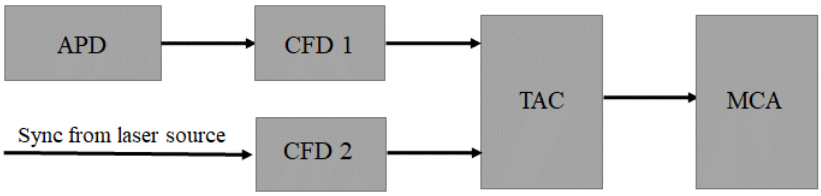

Figure 3.2: Diagram of TCSPC card. APD: avalanche photodiode; CFD: constant fraction discriminator; TAC: time to amplitude converter; MCA: multi-channel analyzer.

The two CFDs is be used to avoid the fluctuation of the amplitude of the electric pulses. Neither too low nor too high amplitude of the electric pulses can pass through. The CFD receiving signal pulses from the pToFS will start the clock of time-to-amplitude converter (TAC) while the other CFD acquiring the synchronization pulse will stop the clock, since a photon is not of 100% probability to be detected for each pulse. A conventional TAC is a current switch capacitor. The current is switched on when the clock is started and the current is switched off when the clock is stopped. The amplitude of the voltage is proportional to the time delay. The output pulses of TAC are sent to a multi-channel analyzer (MCA). The broadening pulse shape can be generated from the accumulation of the arrival time of the photons.

The pToFS provides results quickly by applying MC simulation to the time-broadened pulses, but it is not very precise for phantoms with high absorption or scattering coefficients. The precision is also limited by the simulating program itself.

3.1.2 Collimated transmission spectroscopy

The collimated transmission spectroscopy (CTS) is adopted to characterize the absorption spectrum of the absorbers used in the phantoms. This also validates the pToFS system, from which the absorption coefficient (μ_a) and the reduced scattering coefficient (μ_s') are extracted.

The diagram of the CTS system is shown in Figure 3.3.

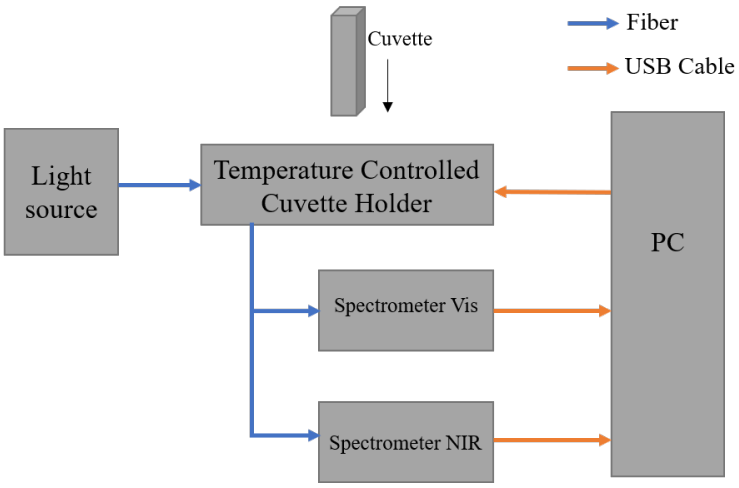

Figure 3.3: CTS setup. The sample is placed in a cuvette and the cuvette is put into a temperature controlled holder. The transmitted light is collected by two spectrometers and analyzed by the computer.

The principle of CTS is to measure the transmitted light attenuated by the sample in the cuvette. This attenuation may come from absorption and scattering effects. By comparing to reference valve of pure water and eliminating the background noise, the transmission T can be written as

$$T = \frac{S - B}{R - B} \tag{3.1}$$

where S is the acquired signal, B is the background spectrum of the spectrometers with the light source off, and R is the reference signal of pure deionized water.

The light source used in CTS is a continuous light source (Tungsten Halogen Light Source, HL-2000-FHSA) emitting broadband light from 360 nm to 2400 nm. The maximum output power is 7 W. The light source needs to warm up before any measurements and a fan is used to cool the instrument. There is an attenuator and a shutter so the output light intensity can be adjusted. The output light is coupled into a multi-mode fiber (Thorlabs M41L02) of a diameter 600 µm. The fiber transmits the light into a cuvette placed in a temperature controlled cuvette holder (Ocean Optics QPOD 2e) which keeps the temperature unchanged during the measuring process. The temperature controller is connected to the PC and the software Q-Blue can detect and adjust the temperature. The incoming light goes through an attenuation slit with 4 mm width and the output light comes from a 2 mm slit. Two collimated lens are utilized to couple the transmitted light into a bifurcated fiber where the transmitted light is split and sent into two different spectrometers. one spectrometer works in

the visible range (Ocean Optics, QE65000) with a spectral range between 200-1100 nm, a bandwidth of 6 nm and an integration time of 8 ms to 5 min. The other spectrometer is a NIR spectrometer (Ocean Optics, NIRQuest512) with a wavelength range between 900-1700 nm, a bandwidth of 3 nm and an integration time of 1 ms-120 s.

3.1.3 Photoacoustic imaging

The photoaoustic imaging setup (Vevo LAZR-X, FUJIFILM VisualSonics Inc., Toronto, Canada) located at the Department of Ophthalmology, Clinical Sciences Lund, Lund University, was used in this thesis project. A photo of the setup is shown below.

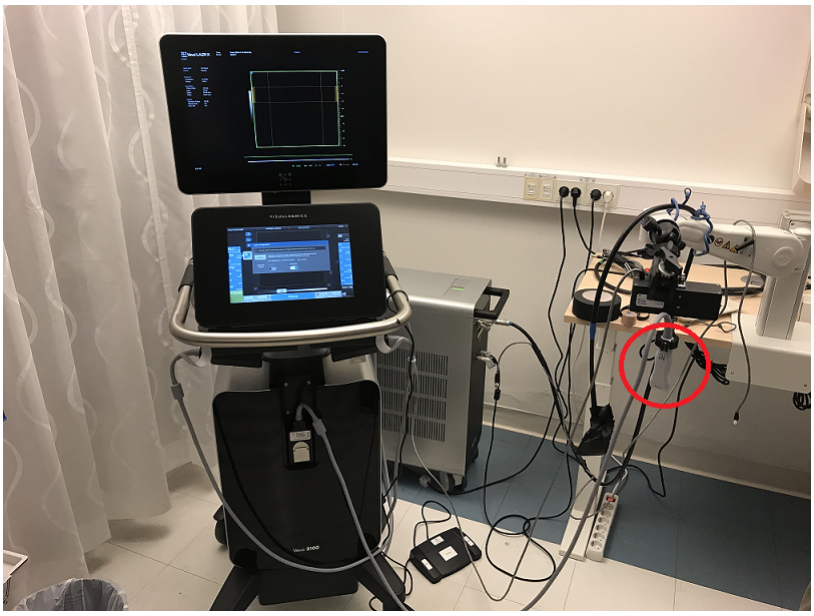

Figure 3.4: Photoaoustic imaging setup. To the left is a screen to show acquired images and a touch screen for operation. Inside the red ring is the transducer. The black box in the back of the machine is the laser source

PAI is an imaging technique based on the photoacoustic effects. After launching a laser pulse into biological tissue, some part of energy is absorbed and converted to heat which causes a thermal expansion of the medium. Then the tissue cools down and the pressure changes during expansion and relaxation result in ultrasound emission. The ultrasound emission can be collected to reconstruct the image of the tissue. Combining the advantages of both optical and acoustic methods, PAI is more sensitive and it is typically two orders of magnitude higher than for normal optical methods [30]. Due to the low absorption and scattering of ultrasound waves in tissue, PAI also provides a better spatial resolution and a larger depth of penetration.

The light source provides near-infrared light at wavelengths between 680 nm to 970 nm at a repetition rate of 20 Hz with a nanosecond pulse width [31]. All the operating process is controlled by computer and the researcher can operate it on a touch screen. The system can work either in pure ultrasound B-mode and in light induced PAI mode. 3D reconstructed images can be acquired by scanning through all three dimensions.

3.2 Characterization of absorbers and scatterers

3.2.1 Absorption of India ink

The CTS was used to characterize the absorption properties of India ink. There are different brands of India ink and their production conditions are subject to change. Hence, a precise characterization of India ink is needed before using it as absorber in phantoms.

The actual measurements were done as follow. First, an ink base was made by dissolving pure India ink in deionized water. The volume concentration of pure ink in the base is denoted as C_0 so the absorption coefficient of the ink base μ_{base} equals to

$$\mu_{base} = C_0\mu_{ink} + (1 - C_0)\mu_{water} \tag{3.2}$$

Then, a series of cuvettes were prepared by adding increasing volumes of ink base into fixed volume of deionized water. The volume concentration of ink base in the whole cuvette is denoted as

$$C = \frac{V_{base}}{V_{base} + V_{water}} \tag{3.3}$$

here C is different for every cuvette and the calculation result from each cuvette can be averaged to be more precise. The absorption coefficient of the whole sample in the cuvette can be written as

$$\mu_{tot} = C\mu_{base} + (1 - C)\mu_{water} \tag{3.4}$$

The cuvettes series was measured by CTS. After recording the dark background of the spectrometers (B), the reference values (R) for pure deionized water and the measured signal from the sample in the cuvette (S), comparing Eq 2.4 and Eq 3.1, the transmission T can be rewritten as

$$\begin{aligned} T = \frac{S - B}{R - B} &= \frac{I_0 e^{-\mu_{tot}L}}{I_0 e^{-\mu_{water}L}} \\ &= e^{-(\mu_{tot} - \mu_{water})L} \\ &= e^{-(C\mu_{base} + (1-C)\mu_{water} - \mu_{water})L} \\ &= e^{C(\mu_{base} - \mu_{water})L} \end{aligned} \tag{3.5}$$

where L is regarded as the thickness of the cuvette, that is 1 cm.

From above, we have

$$\begin{aligned} \mu_{base} &= -\frac{\ln T}{CL} + \mu_{water} \\ \mu_{ink} &= -\frac{\ln T}{C_0 CL} + \mu_{water} \end{aligned} \tag{3.6}$$

3.2.2 Scattering of Intralipid

For Intralipid, the absorption effects was neglected but the scattering effects also attenuate the incoming light. Similar measurements can be perform on cuvettes made of Intralipid in deionized water to acquire the scattering coefficient (μ_s) of Intralipid.

3.2.3 Validation of pToFS

Liquid phantoms consisting of deionized water, India ink base and Intralipid 20% were made to test the pToFS system. Validation was done by comparing the fitting results from pToFS and the measured result from CTS.

A series of liquid phantoms as shown in the Table 3.1 was used for validation. Each phantom measurement was performed three times and the fitting result were extracted to do an average. Higher concentration was not reached since tryout has shown that when the absorption of the phantom was too strong, less attenuation from VOA was needed and the signal-to-noise ratio was too low.

Table 3.1: Liquid phantoms used for validation of pToFS.

Number	Deionized water (mℓ)	Intralipid 20% (mℓ)	1:100 ink base (mℓ)
1	250	1	1
2	250	2	1
3	250	3	1
4	250	4	1
5	250	5	1
6	250	6	1
7	250	7	1
8	250	8	1
9	250	9	1
10	250	10	1
11	250	10	2
12	250	10	3
13	250	10	4
14	250	10	5

Phantoms No.1-10 and No.10-14 were used to study the relation of fitting result from pToFS with Intralipid 20% and ink base concentration, respectively. Phantom No.10 was measured at multiple wavelengths and different source-detector separations (SDS) in particular to evaluate the pToFS data.

3.3 Phantom preparation

3.3.1 General SEBS phantom production

SEBS phantoms were manufactured by the following steps. SEBS powder (Kraton G1650 EU) was first mixed with paraffin oil (Trikem Vet, 5 liter) in the beaker by a mass concentration of 8% [25]. Absorbers and scatterers were then added into the mixture. A magnet was put into the beaker to stir the mixture. The mixture was then heated up to 130°C for 30 to 40 minutes and kept stirring. The SEBS powder would

be dissolved thoroughly in the oil and the mixture became clear and uniform. Ideally, a transparent and homogeneous gel with few bubbles would be obtained. The gel was then poured into molds to shape and cool down.

In this project, a series of phantoms were made to show that the optical properties of SEBS phantoms can be varied. Oil-based colored ink (Cranfield Relief ink) [24] was chosen as absorbers. Three colors, Prussian blue (PB) No.240635, Light green (LG) No.426865 and Rubine magenta (RM) No.634695, were chosen. Tryouts have suggested that pure ink would not be uniformly dispersed in the gel mixture and tiny pieces corresponding to small mass concentration were also hard to handle. Hence, these inks were first dissolved in turpentine to form homogeneous ink bases rather than adding them into the SEBS-paraffin oil mixture directly. The recipes of the three colored ink and turpentine bases are shown in Table 3.2.

Table 3.2: Recipes of three colored ink-turpentine bases.

Color	Ink mass (g)	Turpentine mass (g)	Concentration (%)
PB	0.4819	100.20	0.48
LG	0.4712	99.00	0.47
RM	0.5462	100.83	0.54

The recipes used to manufacture slab SEBS phantoms with enhanced optical properties are shown in Table 3.3. Three colored ink turpentine bases were used as absorbers and TiO_2 was used as scatterers.

Table 3.3: Recipes of SEBS phantoms with colored inks.

	1	2	3	4	5
PB					
SEBS powder (g)	4	4	4	4	4
Ink-Turpentine base (g)	1.09	2.09	3.00	4.00	5.00
Total mass (g)	52.10	50.02	50.01	50.07	50.00
Ink concentration (%)	2.10	4.19	6.00	7.99	10.01
LG					
SEBS powder (g)	4	4	4	4	4
Ink-Turpentine base (g)	1.00	2.04	3.01	4.05	5.02
Total mass (g)	50.02	50.06	51.27	50.09	50.06
Ink concentration (%)	2.00	4.07	5.85	8.08	10.04
RM					
SEBS powder (g)	4	4	4	4	4
Ink-Turpentine base (g)	1.05	2.03	3.01	4.00	5.01
Total mass (g)	50.39	50.09	50.05	50.11	50.20
Ink concentration (%)	2.08	4.06	6.01	7.99	9.98
TiO_2					
SEBS powder (g)	4	4	4	4	4
TiO_2 (g)	0.0061	0.0153	0.0202	0.0312	0.0403
Total mass (g)	40.04	40.06	40.02	40.04	40.05
TiO_2 concentration (%)	0.0152	0.0382	0.0505	0.0779	0.1006

3.3.2 PAI phantoms

A layered cylinder shape SEBS phantom and a big volume cuboid box SEBS phantom were made and measured by the PAI system. The layer phantoms had four thin layers, from top to bottom were SEBS with colors RM, LG, PB and a clear layer. Small part of the mixture gel of three colors was used to form the layer. The box phantom was made by first creating a box shape background SEBS phantom with three cylinder spaces. Only TiO_2 was added to the background SEBS to introduce scattering effects. Then the three cylinders spaces were filled with the other part of the colored gel, so that the three colored layers of the layered phantoms and the three cylinder inclusions of the box phantom shared exactly the same recipe as shown in Table 3.4.

Table 3.4: Recipes of SEBS phantoms for PAI.

Component	SEBS powder (g)	TiO_2 (g)	Ink-Turpentine base (g)	Total mass (g)
Background SEBS	32	0.1537	0	400
PB	4	0	2.99	50.19
LG	4	0	3.06	50.09
RM	4	0	3.04	50.05
Clear SEBS	4	0	0	50.03

Chapter 4

Results and discussion

4.1 Absorption of India ink

Three different brands of India ink were used: the Royal Talens, Rotring and Staedtle, as shown in Figure 4.1.

Figure 4.1: Three brands of inks. From right to left: Royal Talens, Rotring and Staedtler.

Before being measured by the CTS, the Royal Talens ink was first diluted into deionized water to make three ink bases. The concentration of pure ink in water are 1:100, 1:200 and 2:200 in volume fraction. The Rotring and Staedlter India inks were diluted into deionized water with an ink to water ratio of 1:100. By making the assumption that scattering effect of the ink was neglected, the measured extinction coefficient was considered as the absorption coefficient [18].

A series of cuvettes containing different concentrations of ink base was measured. The calculation process was described in Chapter 3 and Eq 3.6 was applied. The actual photo of one of the ink cuvettes series and the calculated transmissions of the samples containing different concentration of Royal talens 1:100 ink base is shown in Figure 4.2 and Figure 4.3.

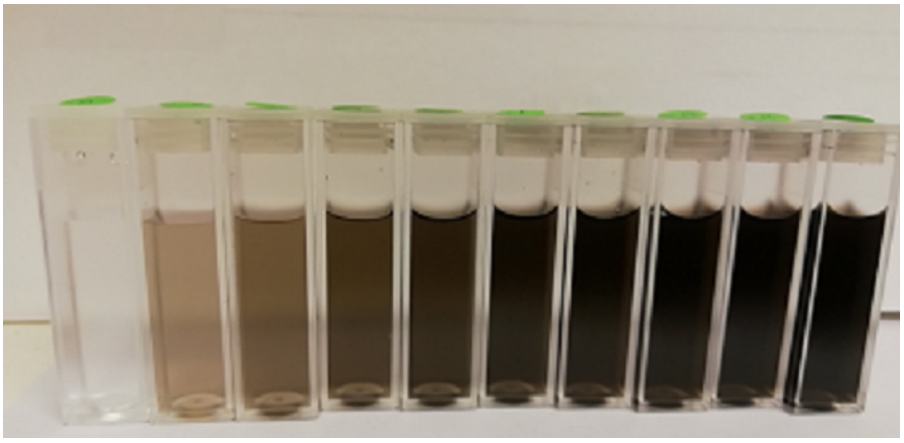

Figure 4.2: Samples with increasing concentration of Royal talens 1:100 ink base, the left one was the cuvette with pure deionized water.

The transmission spectra of the samples is shown in Figure 4.3.

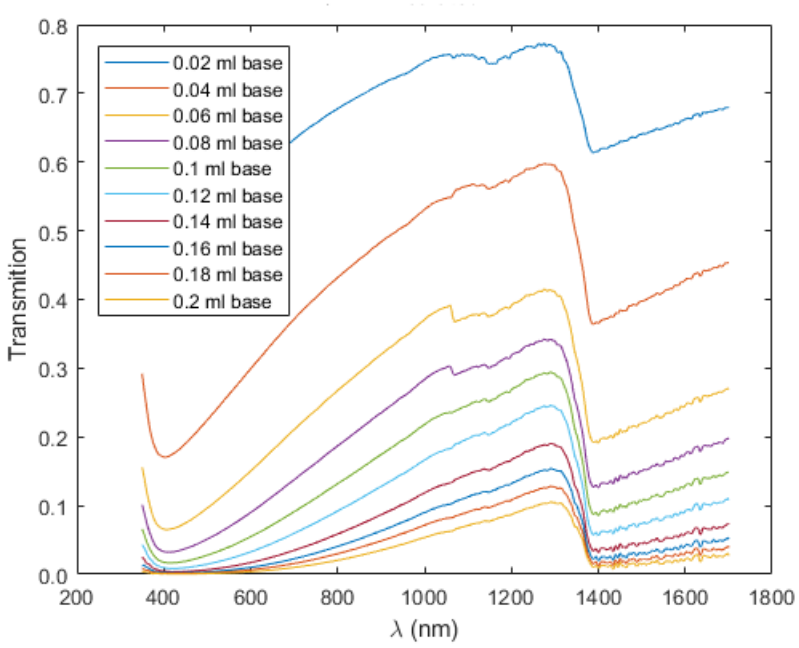

Figure 4.3: Transmission of the samples comparing to pure deionized water.

4.1.1 Royal Talens ink

The mean extinction spectrum of the pure ink calculated from all three ink bases is shown in Figure 4.4. No previous study on this ink was found in related literature.

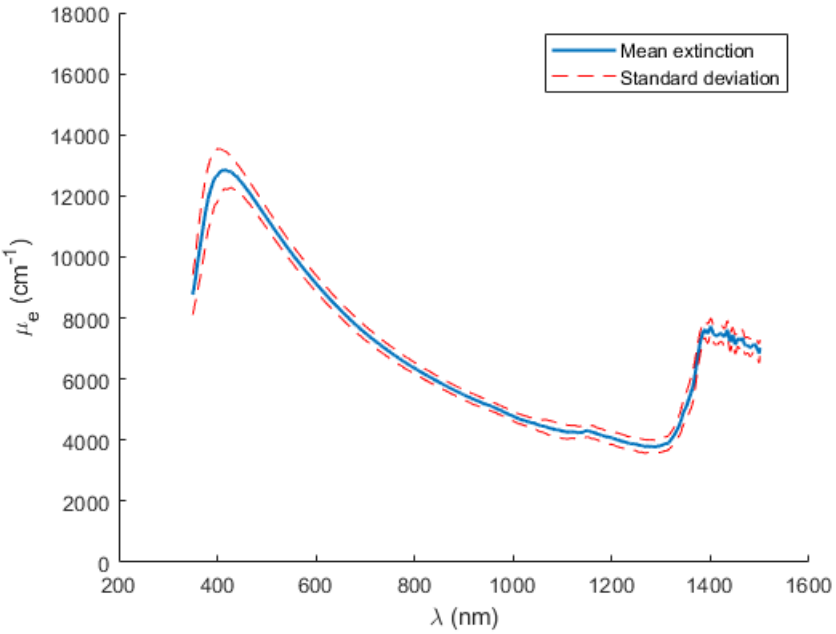

Figure 4.4: Mean extinction spectrum of Royal Talens ink, averaged by all three bases.

The linearity between absorption (μ_a) and ink base concentration for the samples made of three ink bases is shown as below.

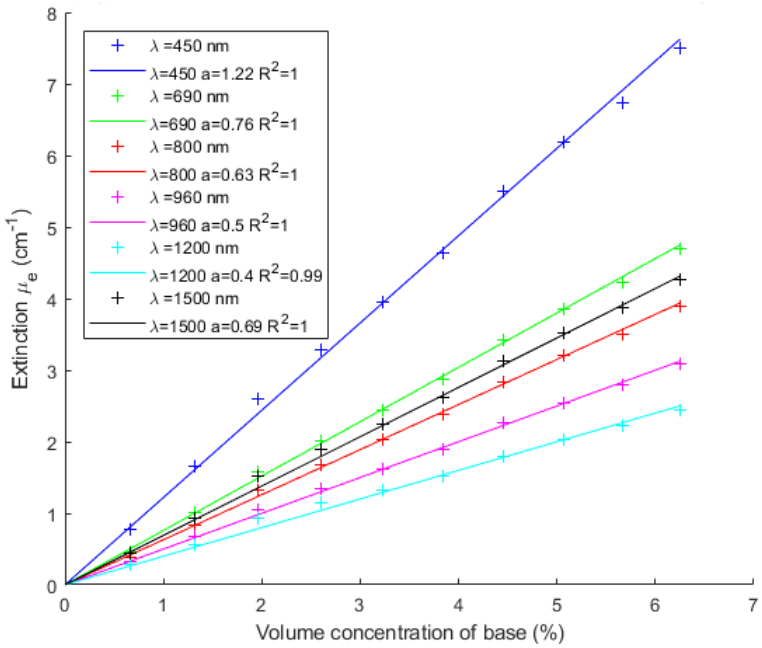

Figure 4.5: Linearity of absorption coefficient (μ_a) to ink base concentration, for the 1:100 base.

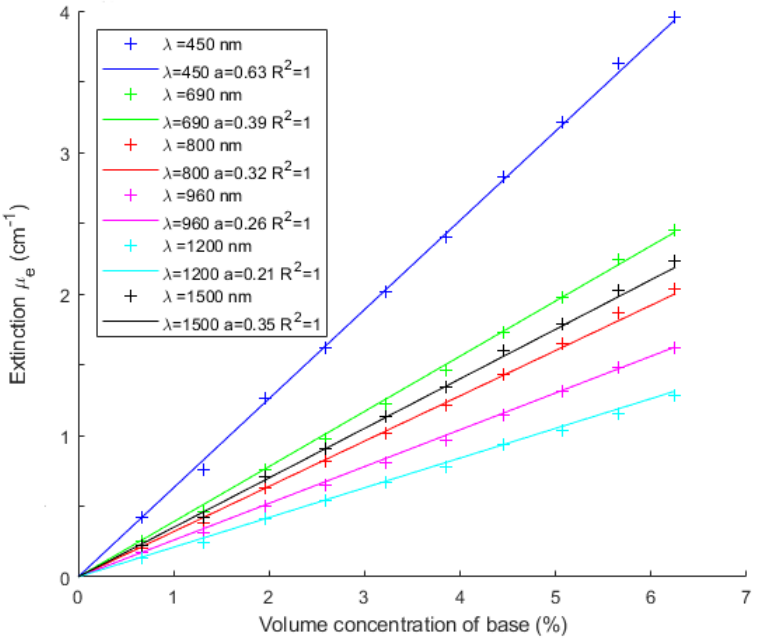

Figure 4.6: Linearity of absorption coefficient (μ_a) to ink base concentration, for the 1:200 base.

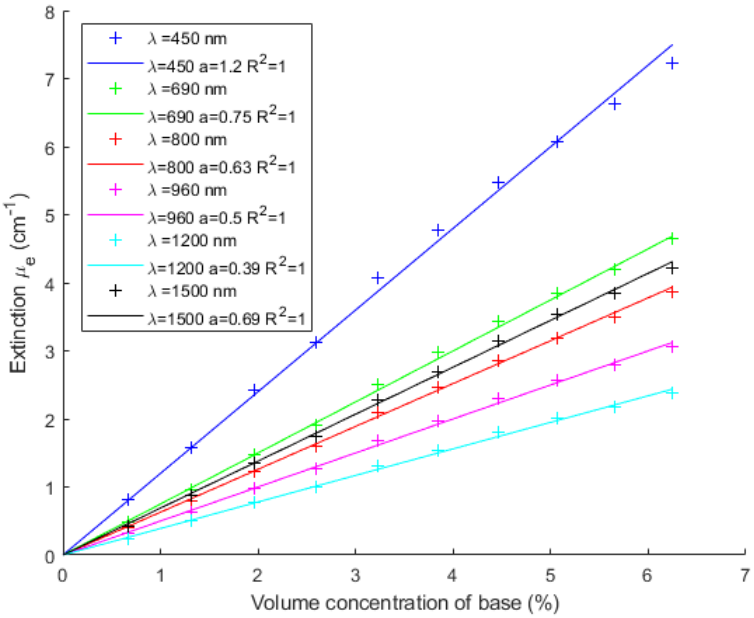

Figure 4.7: Linearity of absorption coefficient (μ_a) to ink base concentration, for the 2:200 base.

4.1.2 Rotring and Staedtler inks

The Rotring and Staedlter India inks were diluted into deionized water with an ink to water ratio of 1:100. Measurements were also done by measuring the samples with different concentration of ink base. The mean extinction spectra of these two brands of ink are shown below. The literature values were estimated from the figures of a previous paper [18].

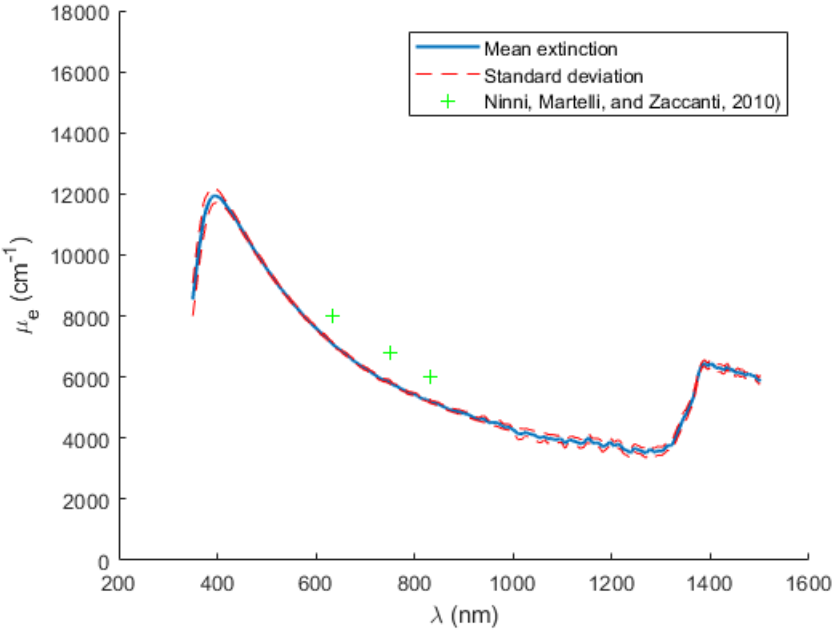

Figure 4.8: Mean extinction spectrum of Rotring ink, measured from 1:100 base.

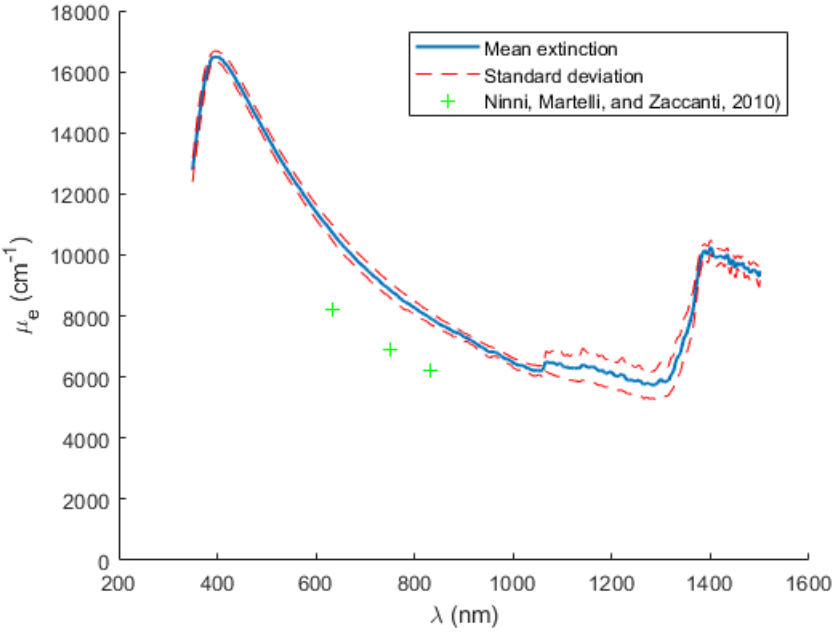

Figure 4.9: Mean extinction spectrum of Staedtler ink, measured from 1:100 base.

The linearity of absorption coefficient (μ_a) of the samples to ink base concentrations of these two brands is shown below.

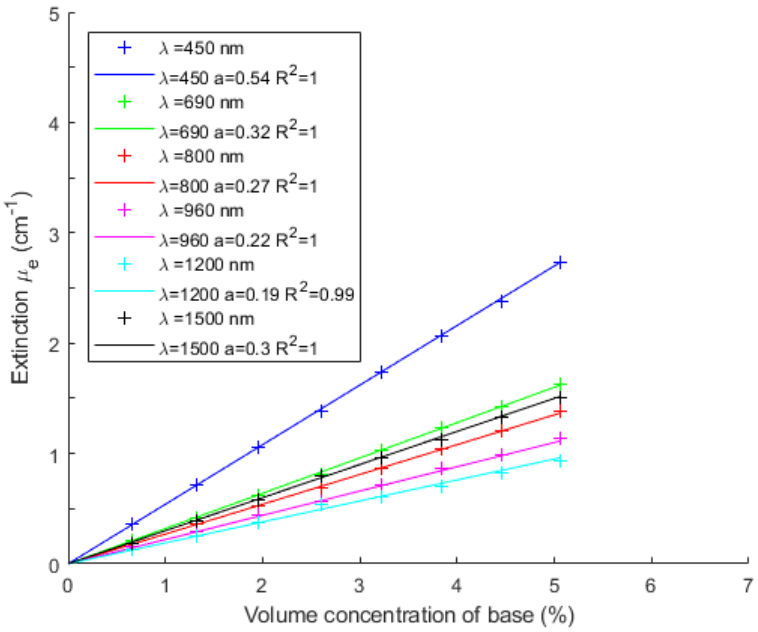

Figure 4.10: Linearity of absorption coefficient (μ_a) to ink base concentration, for the Rotring ink 1:100 base.

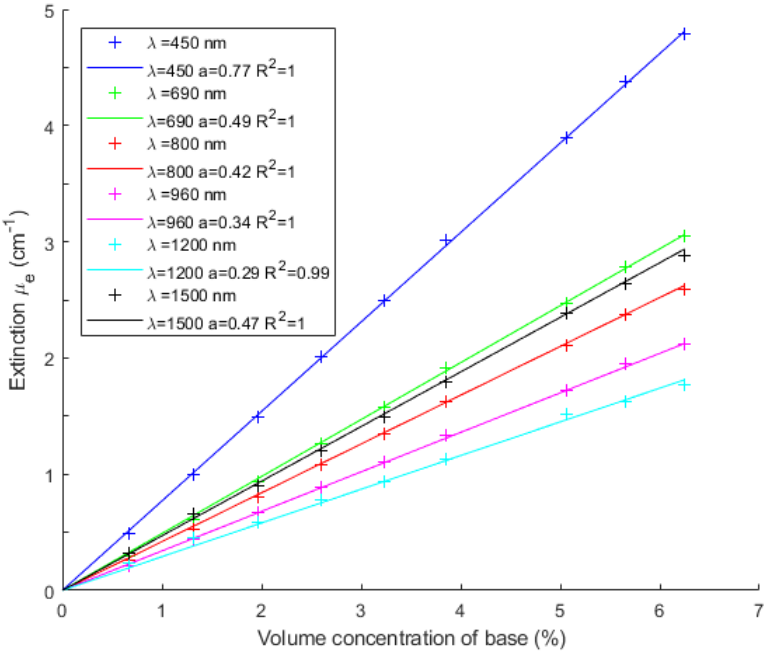

Figure 4.11: Linearity of absorption coefficient (μ_a) to ink base concentration, for the Staedtler ink 1:100 base.

As a small summary, the absorption spectra of all three brands of India ink are shown in Figure 4.12.

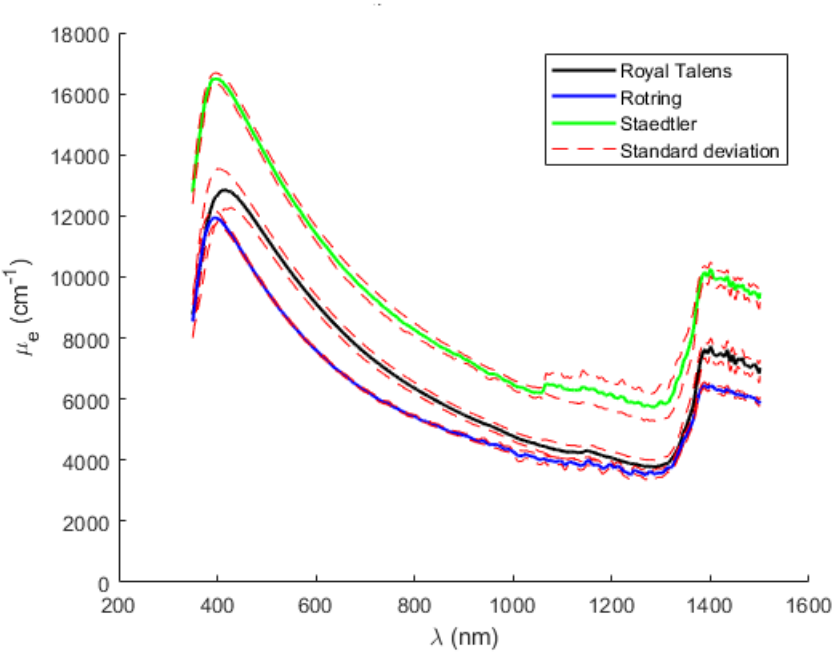

Figure 4.12: Absorption spectra of all three brands of India ink with standard deviation.

Discussion

Unexpected jumps at the beginning and the end of absorption spectra could be found in all the spectra acquired from CTS. The bump in the violet region could be due to the change of cross section in shorter wavelength. While the bump in the NIR region may be due to the absorption water which is not fully eliminated from the signal. There might also be some imprecision from the spectrometers. The absorption coefficient (μ_a) decreases with wavelength increasing. It can be seen that the measured results for these two brands of ink were slightly different to the reported values but they shared the same trend. The difference could come from the usage of various batches of the products and different measuring methods.

As for linearity, there is a good linear relation between μ_a and ink base concentrations for all three brands of ink. For the three ink bases of the Royal Talens ink, the slopes of the linear function and actual μ_a values for the 1:100 and 2:200 base are similar, and they are nearly twice of the values for the 1:200 base, respectively.

4.2 Scattering of Intralipid

The parameter measured by CTS was the extinction of the sample inside the cuvette. By treating the absorption coefficient of Intralipid as water [32], the measured extinction coefficient of the sample was regarded as the scattering coefficient introduced by Intralipid. The result is shown in Figure 4.13 and comparison was made with the green line drawn by Eq 2.15 and typical reference values [32].

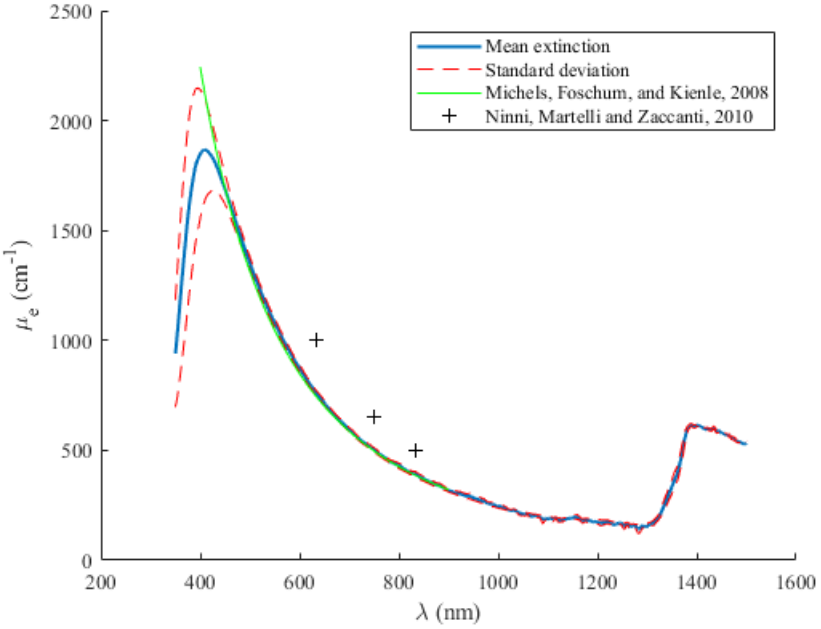

Figure 4.13: Mean extinction spectrum of Intralipid 20%.

The linearity between scattering coefficient (μ_s) and Intralipid 20% concentration is shown in Figure 4.14.

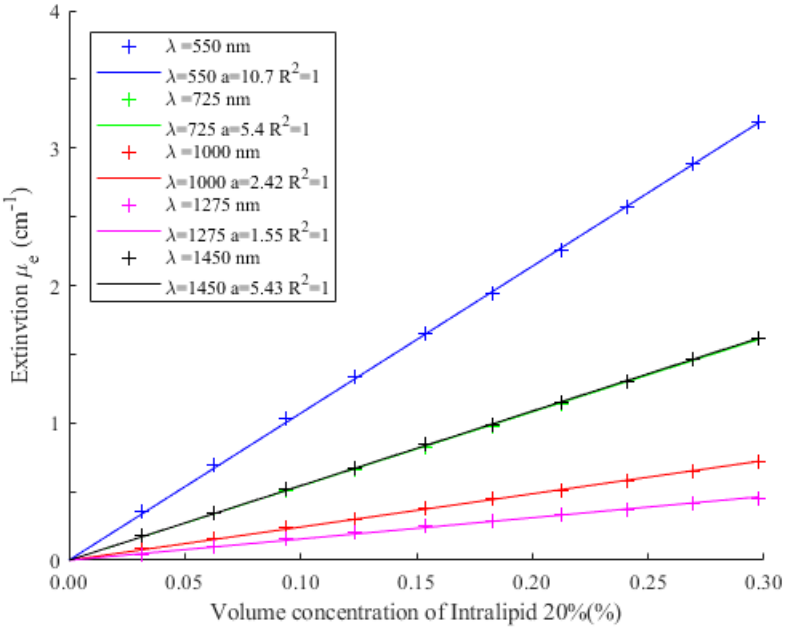

Figure 4.14: Linearity of scattering coefficient to Intralipid 20% concentration.

Discussion

It can be seen that there is a good match of measured results with reference values between 400 nm to 900 nm, where formula Eq 2.15 is valid. However, a bump can

be found from 300 nm to 400 nm. This might be explained as the wavelength of the light here is similar to the size of scattering particles, the scattering cross-section would change so that the scattering coefficient behaves differently. There is a good linearity between scattering coefficient (μ_s) and volume concentration of Intralipid 20% for wavelengths over 400 nm.

4.3 Validation of pToFS

White MC simulation was used for the pToFS system to fit the time-broadened pulse shape [33]. Liquid phantoms mentioned in Chapter 3 were used. Fit results at different ink base and Intralipid 20% concentrations, multiple wavelengths and variable SDS values were studied. The ink extinction spectrum and Eq 2.15 were used to calculate the comparing values.

Concentration

In this section, fit results while changing ink and Intralipid concentrations were studied. The incident wavelength was chosen at 600 nm and the SDS value was 1 cm.

Phantoms No.1 to No.10 were first chosen. The volume of ink base was kept unchanged as 1 mℓ, while the volume of Intralipid 20% was increased by a step size of 1 mℓ from 1 to 10 mℓ.

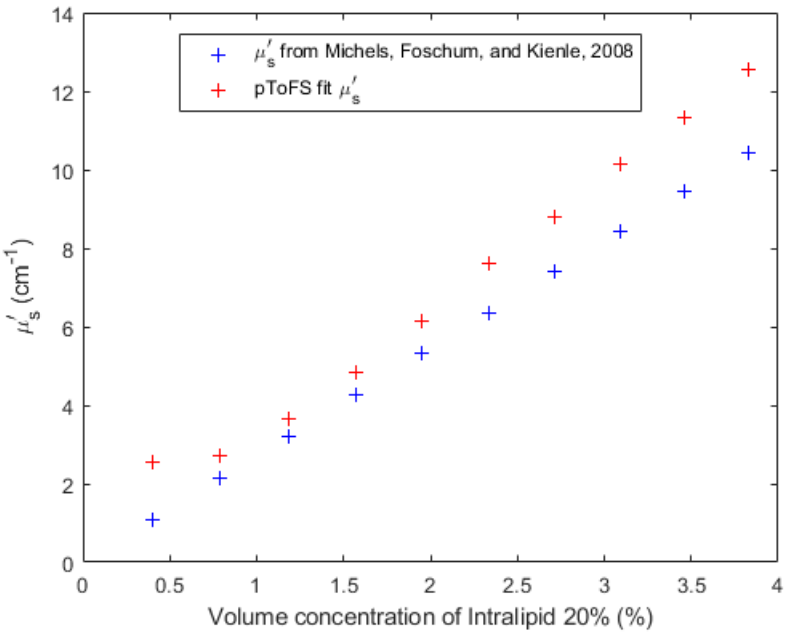

Figure 4.15: Fit result of the reduced scattering coefficient (μ_s') versus Intralipid 20% concentration, when increasing the volume of Intralipid 20%.

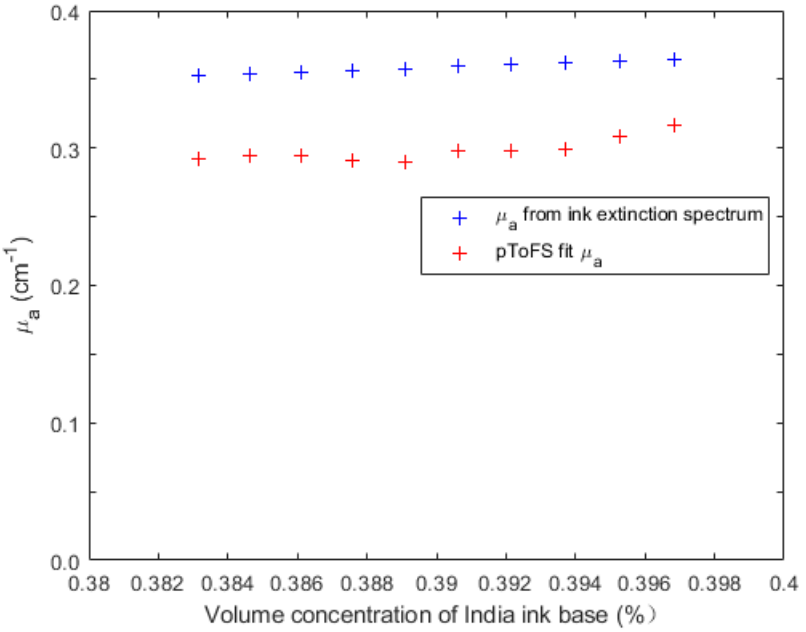

Figure 4.16: Fit result of the absorption coefficient (μ_a) versus ink base concentration, when increasing the volume of Intralipid 20%.

Fit result from liquid phantoms No.10 to No.14 is shown below. The volume of Intralipid 20% was kept unchanged as 10 mℓ, while the volume of ink base was increased by a step size of 1 mℓ from 1 to 5 mℓ.

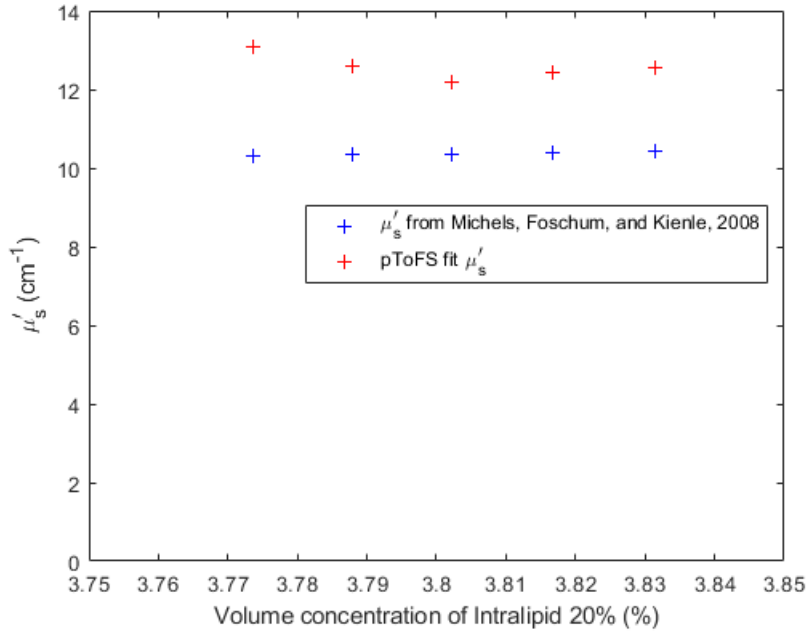

Figure 4.17: Fit result of the reduced scattering coefficient (μ_s') versus Intralipid 20% concentration, when increasing the volume of ink base.

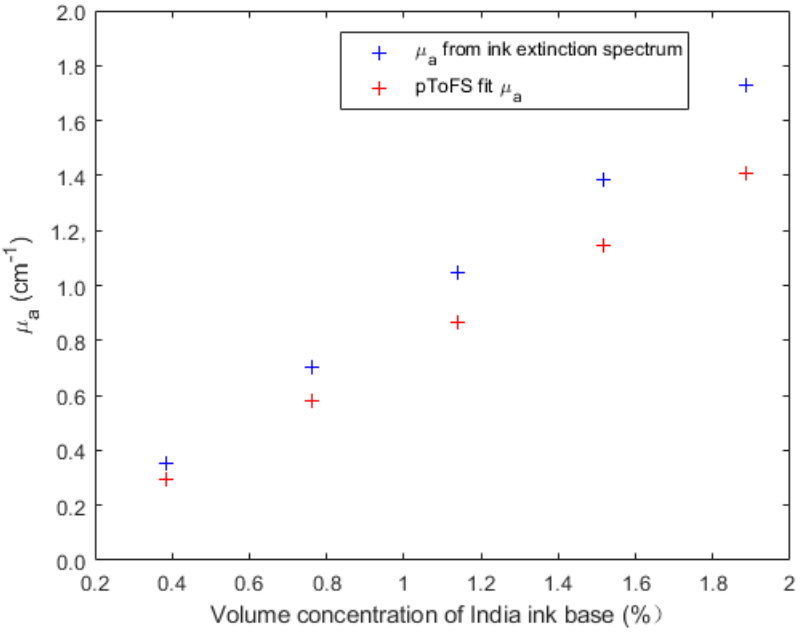

Figure 4.18: Fit result of the absorption coefficient (μ_a) versus ink base concentration, when increasing the volume of ink base.

Wavelength

In this section, liquid phantom No.10, made with 250 mℓ deionized water, 10 mℓ Intralipid 20% and 1 mℓ ink base, was chosen to study the fit result at different wavelengths from 500 nm to 1000 nm at an SDS value of 1 cm.

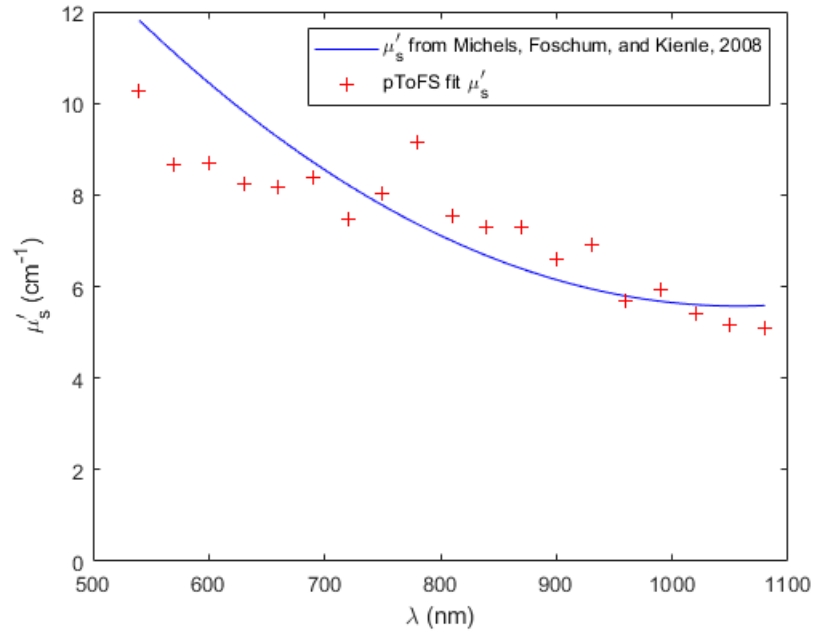

Figure 4.19: Fit result of the reduced scattering coefficient (μ_s') at different wavelengths from 500 to 1100 nm.

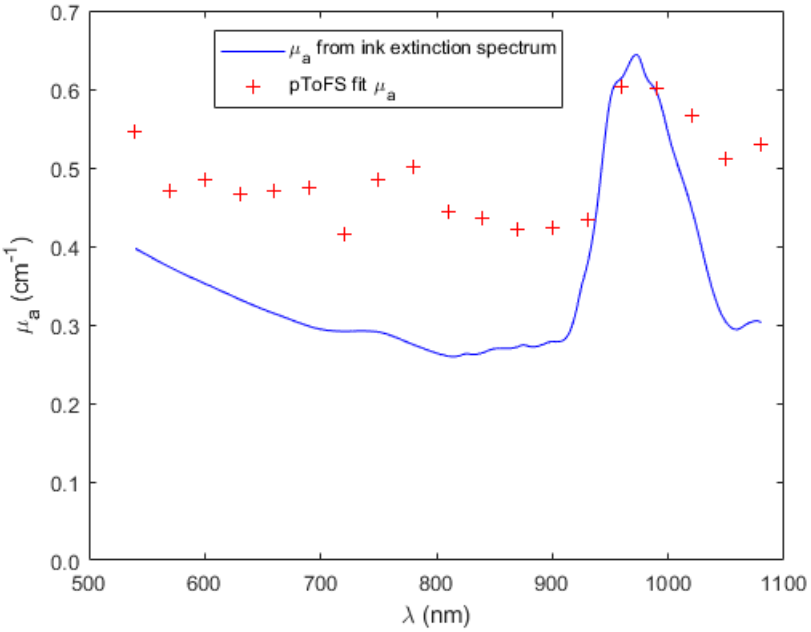

Figure 4.20: Fit result of the absorption coefficient (μ_a) at different wavelengths from 500 to 1100 nm.

Source-detector separation

In this section, liquid phantom No.10, made with 250 mℓ deionized water, 10 mℓ Intralipid 20% and 1 mℓ ink base, was chosen to study the fit result at different SDS values from 0.75 to 2.0 (cm) at wavelength of 660 (nm).

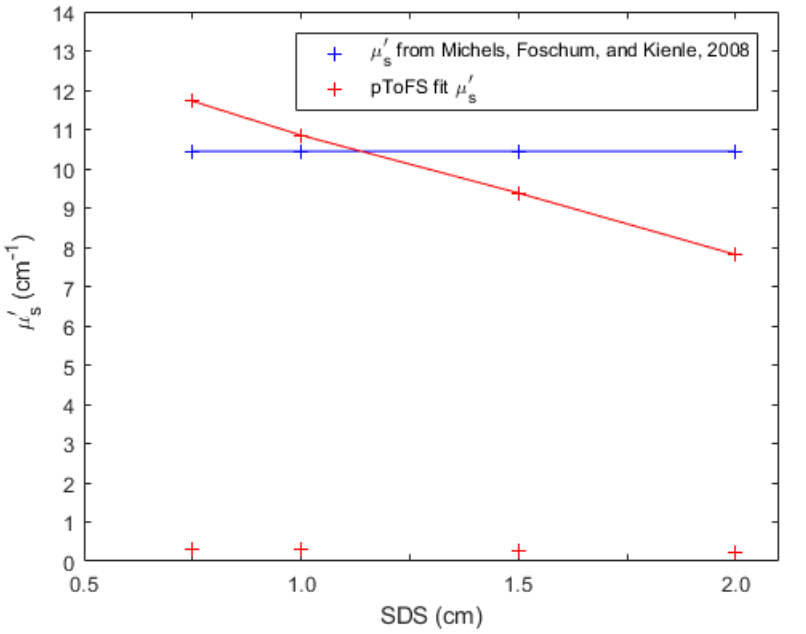

Figure 4.21: Fit result of the reduced scattering coefficient (μ_s') at different SDS values from 0.75 to 2.0 cm.

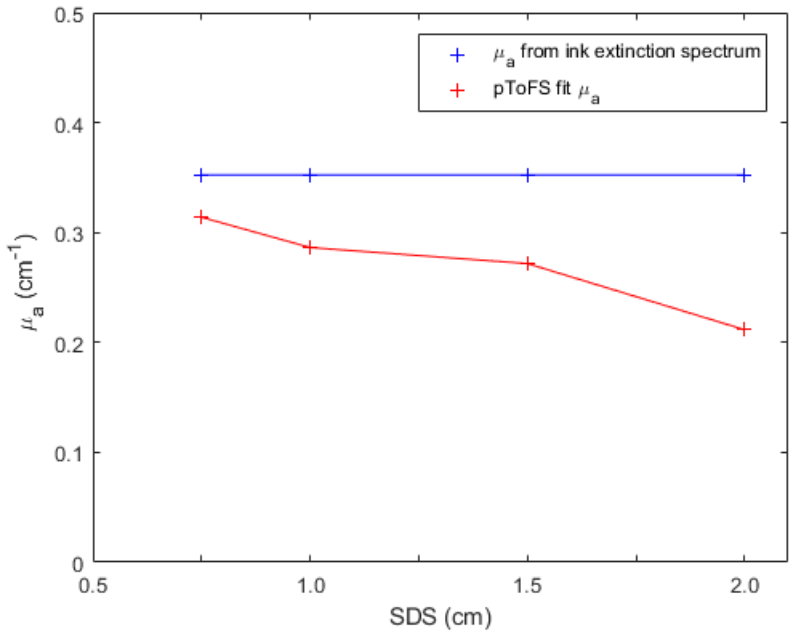

Figure 4.22: Fit result of the absorption coefficient (μ_a) at different SDS values from 0.75 to 2.0 cm.

Discussion

It can be seen from the figures above that, when changing concentrations, fit results from the pToFs system was different from the reference values and the trend of linearity was also obvious. The fitted μ_a was always lower while the fitted μ_s' was always higher thank those of the reference values. This may be explained as the measured μ_a of India ink from CTS is actually composed of both absorption and scattering coefficients, so part of the it is contributing to μ_s' in reality. This suggests that the scattering effects of India ink may not be neglected. For different wavelengths, fit results were not precise but show nearly same trend as reference. However, the results were not consistent at different SDS which means an upgrade of the fitting program is needed.

4.4 SEBS Phantoms with enhanced optical properties

SEBS phantoms with three oil-based colored inks TiO_2 were fabricated and measured with CTS, respectively. Part of the gel was poured into three cuvettes. The remaining part of gel was made into a slab phantom. The results from three averaging samples were similar suggesting that the SEBS phantoms were homogeneous.

4.4.1 Absorption: colored inks

Bases of three colored inks dissolved in turpentine were first measured to characterize the absorption properties. The process was similar to what has been done with the ink base. The absorption spectra of all three colored ink bases are shown in Figure 4.23.

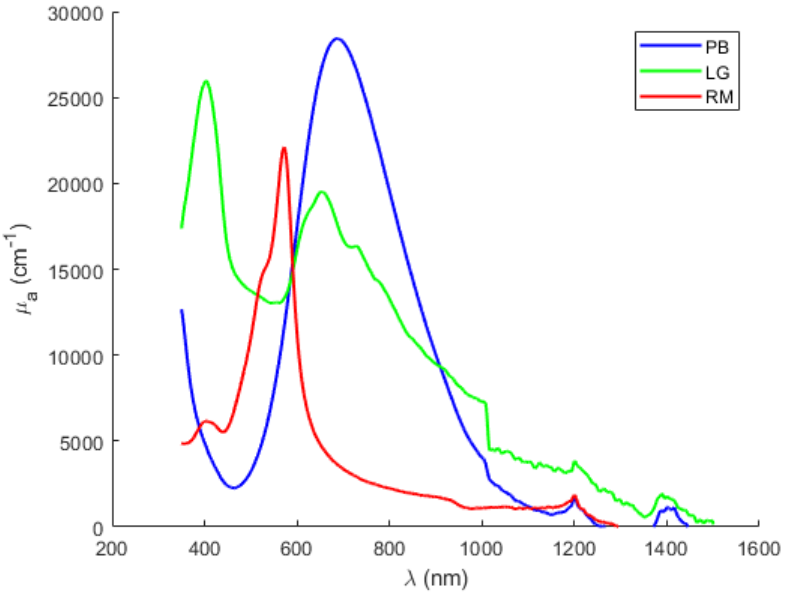

Figure 4.23: Absorption spectra of three colored ink-turpentine bases.

It can be seen that the PB ink has the most strong absorption within the wavelength region of the PAI system. The LG ink also absorbs in this region but at a much lower level. The RM ink barely absorbs at the wavelength region of interest. The PB ink could be promising to be used as absorbers to provide photacoustic signal.

Colored ink: PB

Photos of the cuvettes series filled with PB SEBS phantom and the slab SEBS phantom series are shown in Figure 4.24.

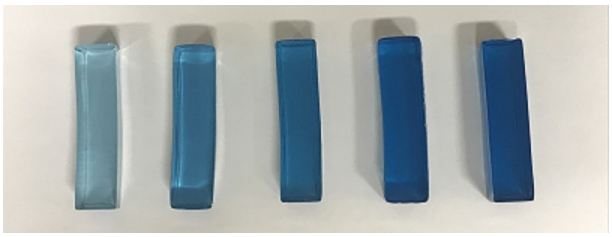

(a)

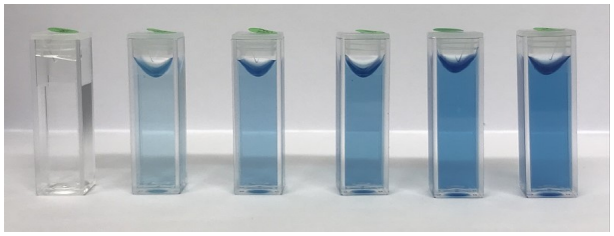

(b)

Figure 4.24: (a) Slab phantom series with increasing concentration of PB ink; (b) Samples with increasing concentration of PB ink. The one to the left is deionized water.

Absorption spectra and linearity relation

The absorption spectra and the linearity of the absorption coefficient (μ_a) with the volume concentration of the PB ink-turpentine base are shown in Figure 4.26.

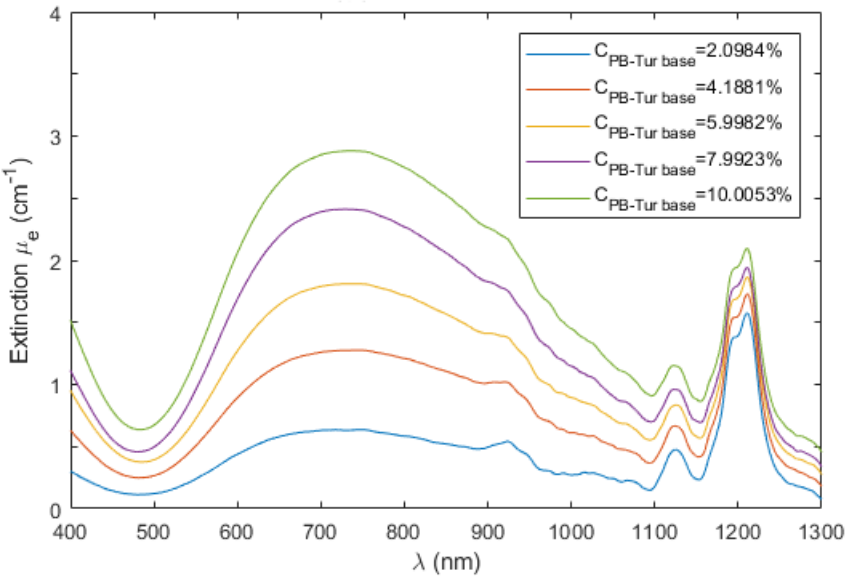

Figure 4.25: Absorption spectra of the PB SEBS series with five different concentrations.

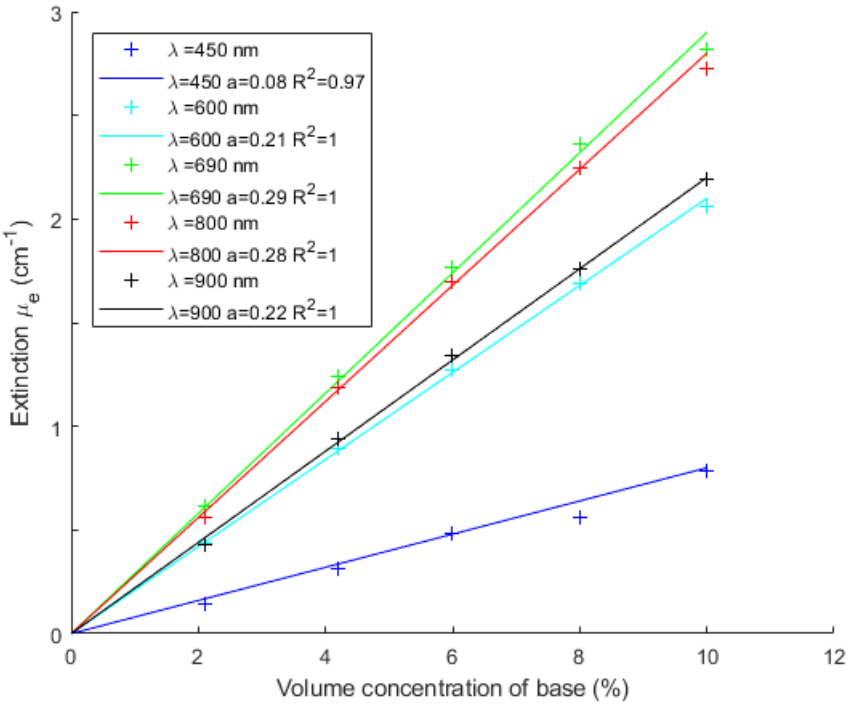

Figure 4.26: Linearity of the absorption coefficient (μ_a) to volume concentration of the ink-turpentine base at five wavelengths.

Colored ink: LG

Photos of the cuvettes series filled with LG SEBS phantom and the slab SEBS phantom series are shown in Figure 4.27.

(a)

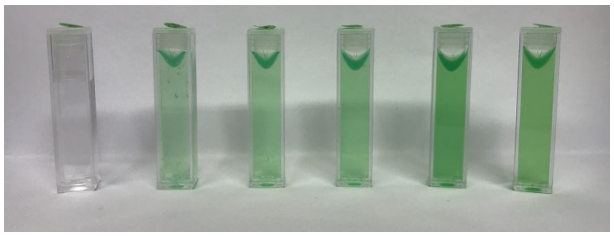

(b)

Figure 4.27: (a) Slab phantom series with increasing concentration of LG ink; (b) Sample series with increasing concentration of LG ink. The one to the left is deionized water.

Absorption spectra and linearity relation

The absorption spectra and the linearity of the absorption coefficient (μ_a) with the volume concentration of the LG ink-turpentine base are shown in Figure 4.29.

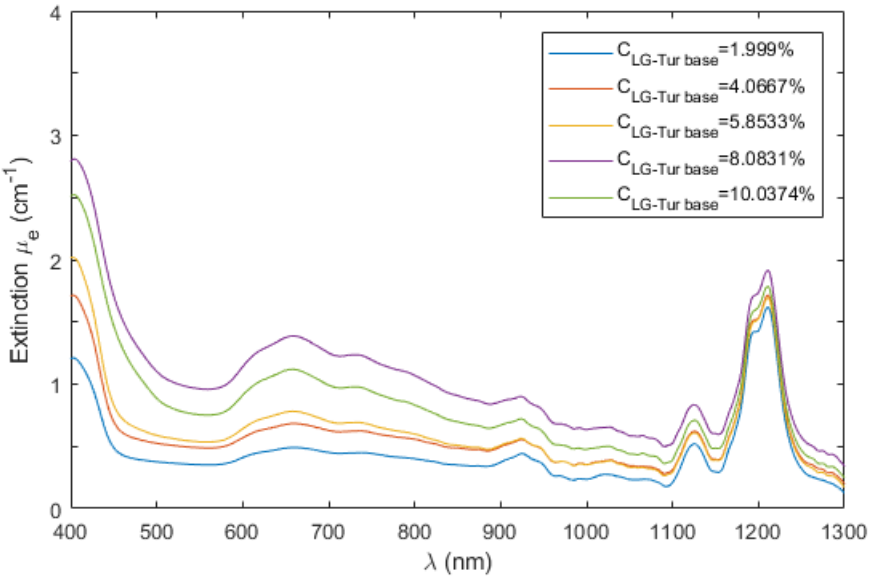

Figure 4.28: Absorption spectra of the LG SEBS series with five different concentrations.

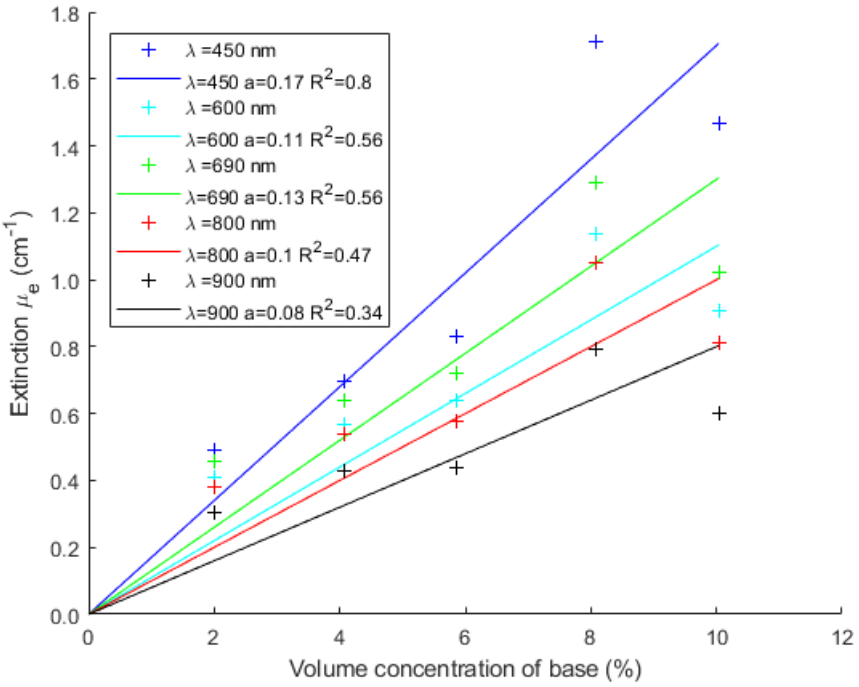

Figure 4.29: Linearity of the absorption coefficient (μ_a) to volume concentration of the ink-turpentine base at five wavelengths.

Colored ink: RM

Photos of the cuvettes series filled with RM SEBS phantom and the slab SEBS phantom series are shown in Figure 4.30.

(a)

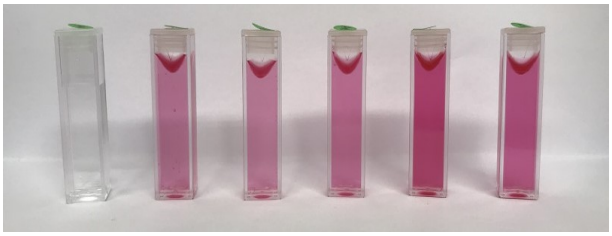

(b)

Figure 4.30: (a) Slab phantom series with increasing concentration of RM ink; (b) Samples with increasing concentration of RM ink. The one to the left is deionized water.

Absorption spectra and linearity relation

The absorption spectra and the linearity of the absorption coefficient (μ_a) with the volume concentration of the RM ink-turpentine base are shown in Figure 4.32.

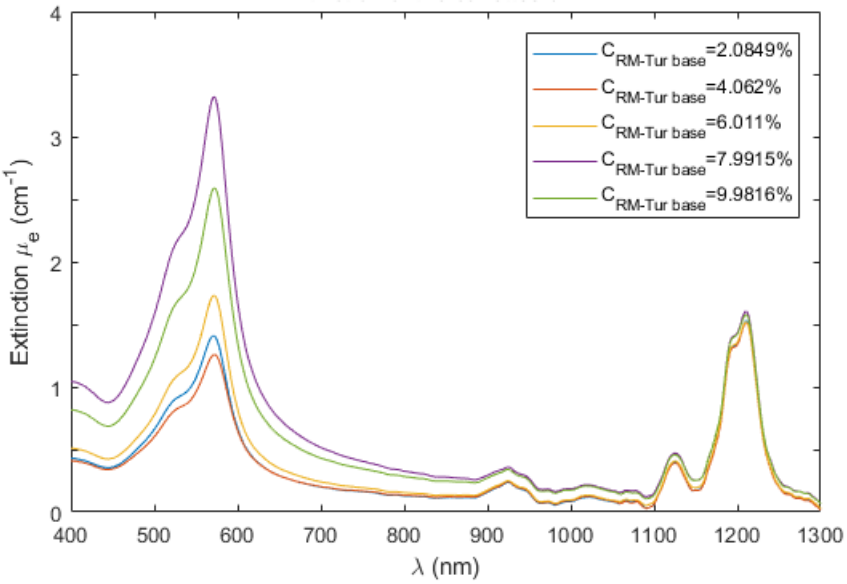

Figure 4.31: Absorption spectra of the RM SEBS series with five different concentrations.

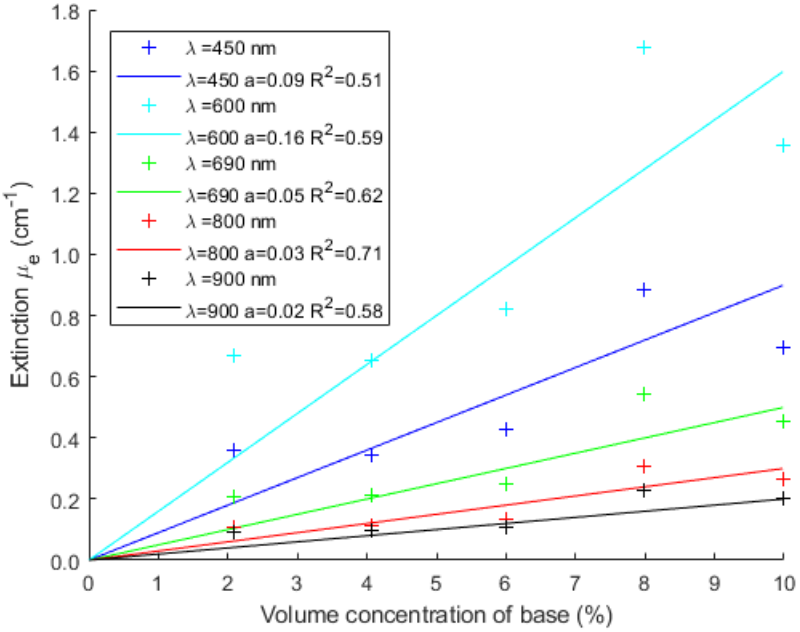

Figure 4.32: Linearity of the absorption coefficient (μ_a) to volume concentration of the ink-turpentine base at five wavelengths.

Discussion

It can be seen from the figures above that the PB ink shows obvious absorption property and precise linearity to ink base concentrations, suggesting that it is very suitable to be used as absorbers in SEBS phantoms for PAI. On the contrary, the linear fittings of the LG ink and the RM ink were not good as expected. This could be the consequence of imprecise handling during fabrication and careless operation while measuring. Repeated measurement could be down.

Scattering: TiO_2

Photos of the cuvettes series filled with SEBS phantom with TiO_2 and the slab SEBS phantom series are shown in Figure 4.33.

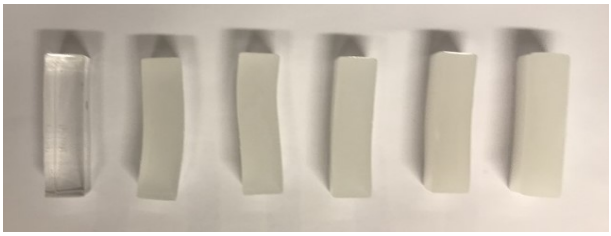

(a)

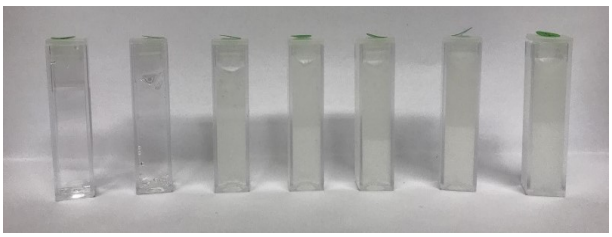

(b)

Figure 4.33: (a) Slab phantom series with increasing concentration of TiO_2; (b) Samples series with increasing concentration of TiO_2. The one to the left is deionized water.

Absorption spectra and linearity relation

The absorption spectra and the linearity of scattering coefficient (μ_s) with mass concentration of TiO_2 of the samples are shown in Figure 4.35.

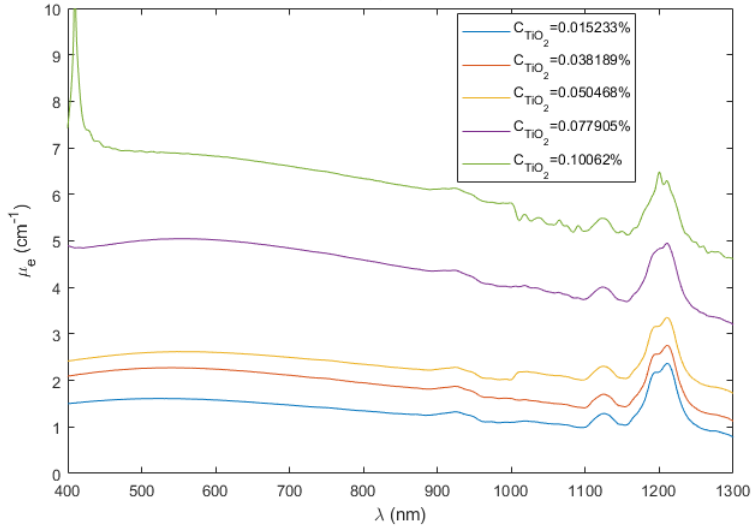

Figure 4.34: Extinction spectra of the TiO_2 SEBS series with five different concentrations.

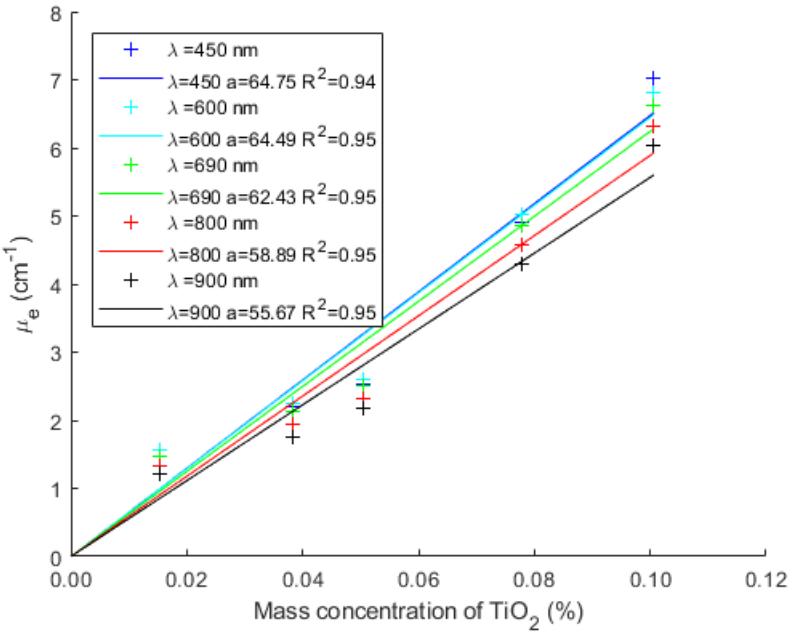

Figure 4.35: Linearity of absorption coefficient (μ_a) to TiO_2 concentration at five wavelengths.

Discussion

It can be seen that TiO_2 provided relatively flat scattering effects over the measured wavelength region. With a relative factor around 0.95, the scattering coefficient (μ_s) of SEBS phantoms showed acceptably good linearity to the mass concentration of TiO_2, indicating that it is possible to tune the scattering coefficient by adding TiO_2.

4.4.2 PAI phantom and the photoacoustic images

SEBS slabs

The colored SEBS slabs with highest concentration of inks were brought to the PAI laboratory. Full spectral scanning was performed on slabs of all three colors and the photoacoustic signal spectra over the whole wavelength region, 680 nm to 970 nm, were acquired. The signal intensity was recorded in an Excel file and imported to Matlab. The photoacoustic signal spectra are shown in Figure 4.36.

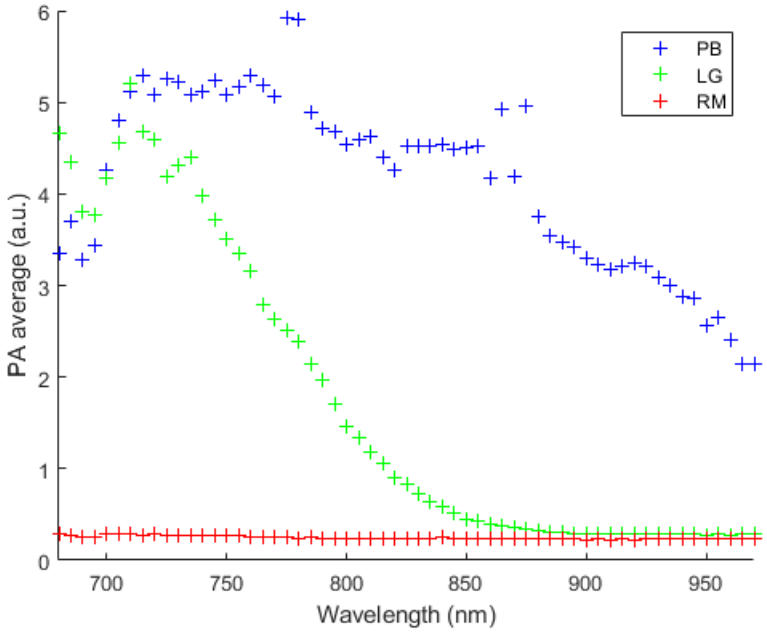

Figure 4.36: Photoacoustic signal intensity spetra of slab SEBS phantoms with three ink colors, respectively.

It can be seen that the SEBS slab made with colored ink PB showed a strong signal over the whole wavelength region and the one with LG presented weaker signal from 680 nm to nearly 850 nm. On the other hand, the RM colored SEBS slab almost did not present any signal but noise throughout the wavelength region. Comparing to Fig 4.23 and the discussion above, it can be concluded that the photoacoustic signal intensity increases with absorption coefficient of the phantom increasing, which correspond to the fact that the photoacoustic effects is induced by the absorption of incident light energy. Higher absorption coefficient means more energy absorbed, hence stronger photoacoustic signal.

A comparison of photoacoustic signal and absorption spectra of all three colors is shown in Figure 4.37 by making the ratio of Figure 4.23 and Figure 4.36.

It can be seen that the ratio value for the PB SEBS slab remains stable over the wavelength region of interest which means the PB color could be a stable and reliable absorber in SEBS phantoms to generate photoacoustic signal.

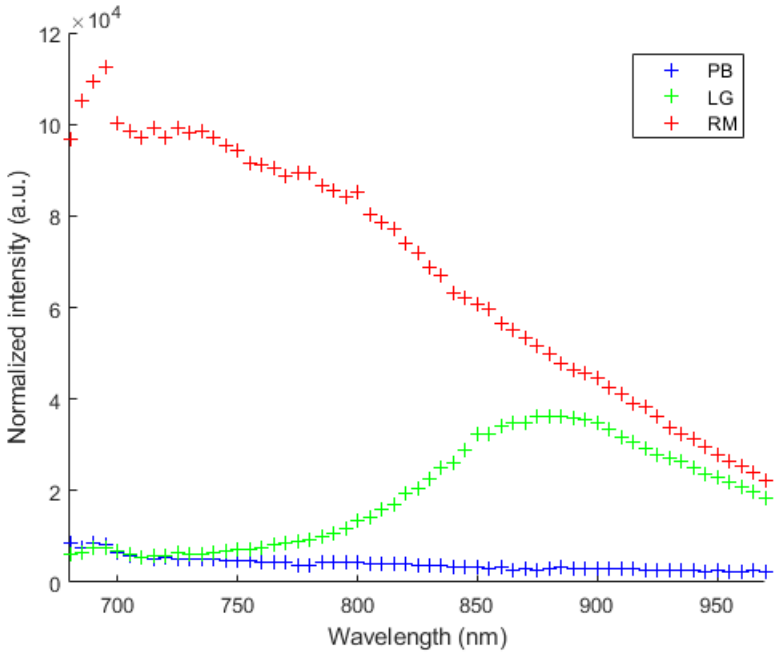

Figure 4.37: The ratio of absorption coefficient (μ_a) to photoacoustic signal intensity (PA average) for all three colors.

Layered SEBS phantom

A four-layer SEBS phantom was made using a cup as the mold. The pictures of the layered phantom being measured is shown in Figure 4.38.

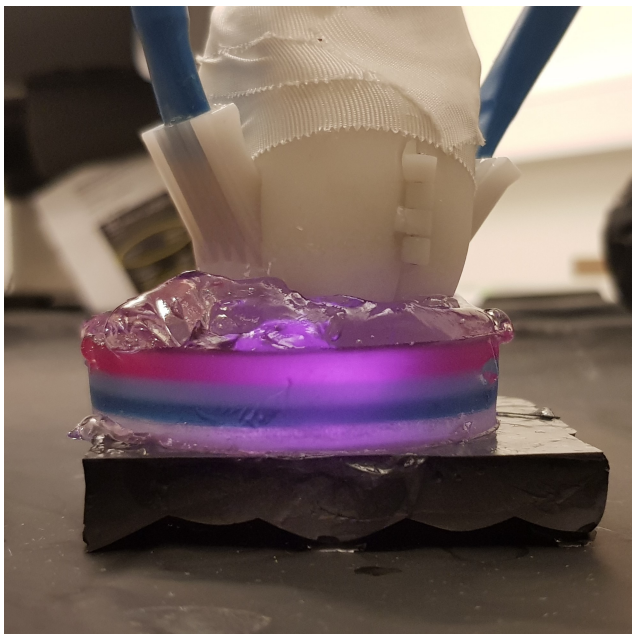

Figure 4.38: Measurement on phantom with four layers: RM, LG, PB and clear SEBS. The transducer brought in the laser pulse and collected the resulting ultrasound emission to form photoacoustic images.

The layers were SEBS with ink of RM, LG, PB and a clear SEBS , from top to bottom. The fiber on the transducer illuminated the phantom and the incident laser would induce that photoacoustic effects. The photoacoustic images were acquired by scanning over the whole wavelength range from 680 to 970 nm. Spectral unmixing was applied in the data analysis so that each colored-layer was shown with true colors.

The photoacoustic images are shown in Figure 4.39.

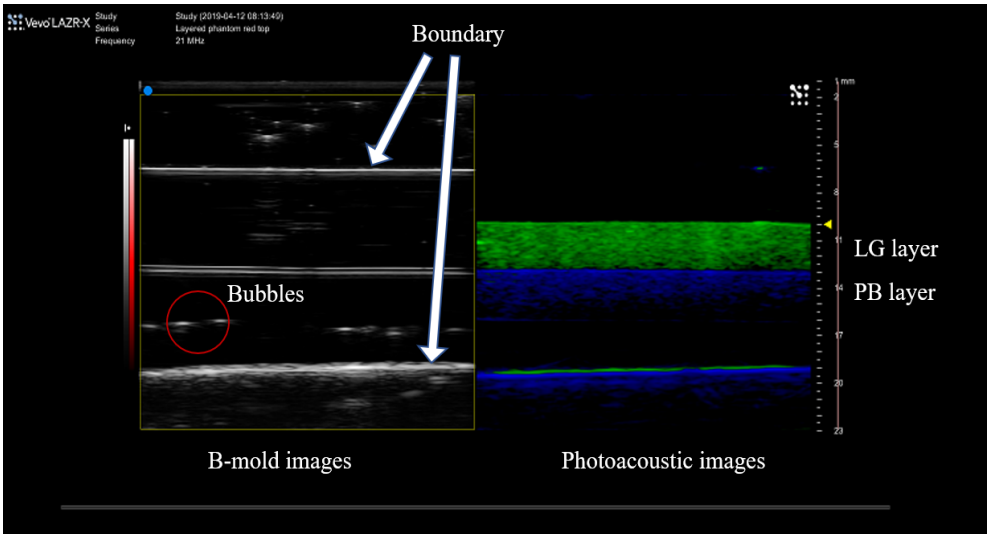

(a)

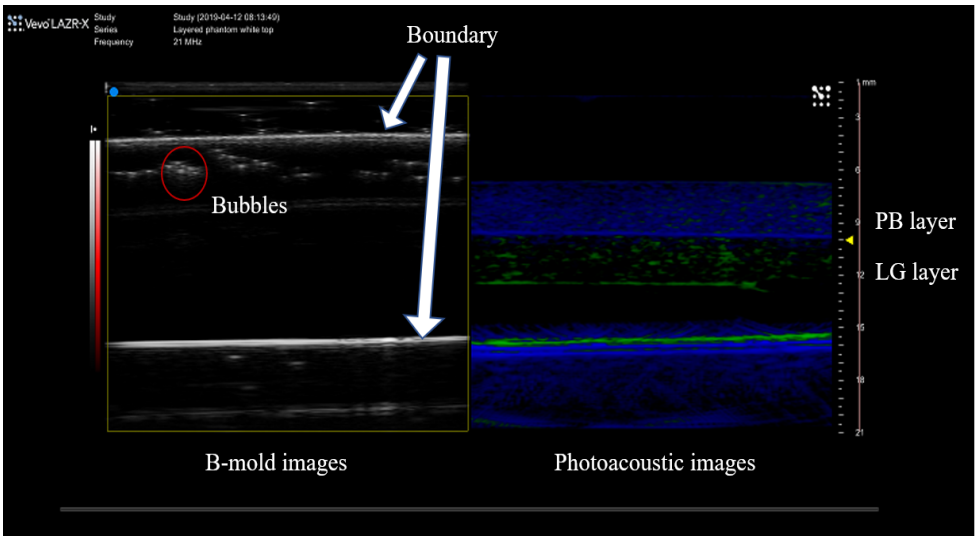

(b)

Figure 4.39: Photoacoustic images: The left of the images were the normal ultrasound B-mode images; The right part were the photoacoustic images. (a) light came in from RM SEBS to clear SEBS; (b) light came in the other way around.

The left part of the picture was the ultrasound B-mode image of the SEBS. The upper and the bottom boundary can be seen and the line in the middle was the boundary between the LG and the PB SEBS. The photoacoustic image on the right side shows the boundary clearly. For image (a), the light was partly absorbed by the

second LG layer so that the signal acquired from the PB layer was not that strong. When changing the incident direction, it can be seen from image (b) that the light was mainly absorbed by the PB layer so the LG layer was almost dark. Both the images showed no obvious signal from the clear SEBS layer and the RM layer. The signal out of the phantom region could be the back-scattered acoustic wave.

Box SEBS phantom with inclusions

A relatively big volume box phantom with scattering background and absorption inclusion was made following the recipe. A Photo of the box SEBS phantom being measured is shown in Figure 4.40.

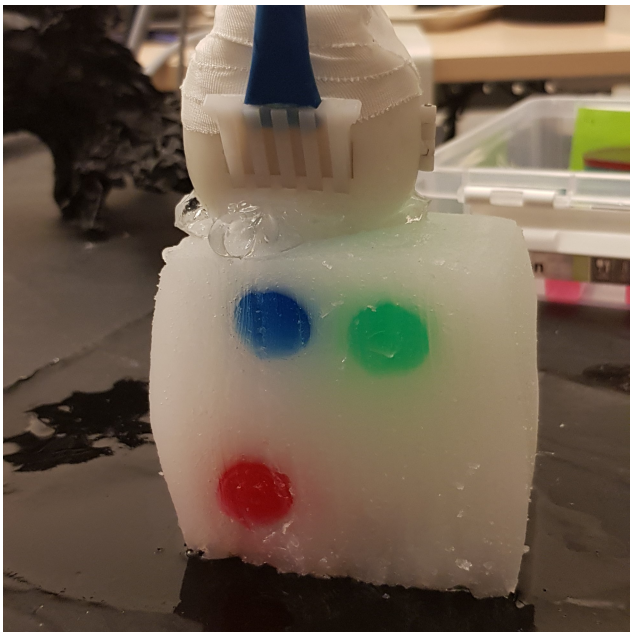

Figure 4.40: Measurement on box phantom with three inclusion: PB, LG and RM. The transducer scanned over the surface to acquire 3D images.

3D scanning and reconstruction was performed to test the ability of showing depth resolution and complex shape of the inclusion. From the previous measurement, it was known that the RM SEBS did not absorb throughout the wavelength region. Hence, the photoacoustic images were taken on the surface close to the PB and LG inclusion. The acquired 3D scanning images are shown in Figure 4.41. Two different wavelengths, 680 nm and 850 nm, were applied to show the visibility of the inclusions.

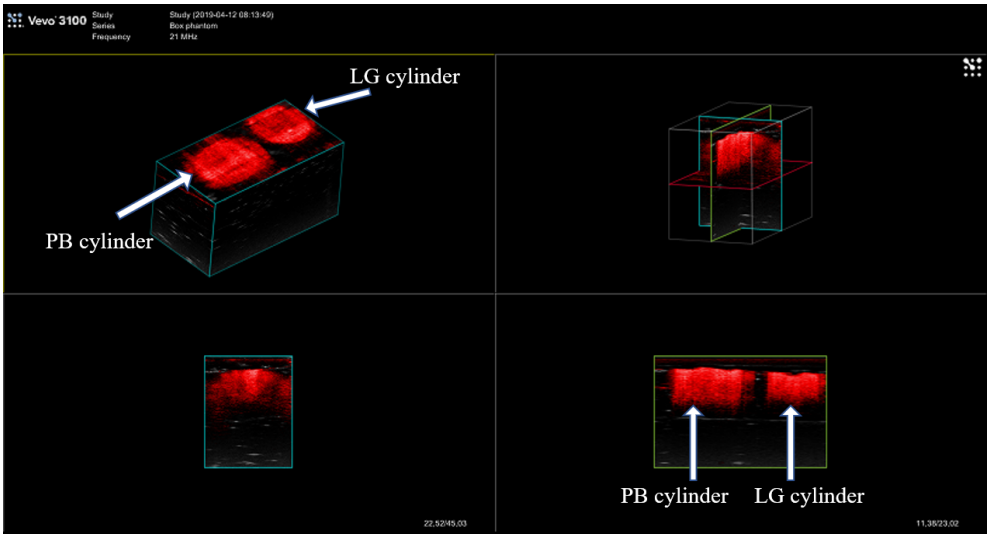

(a)

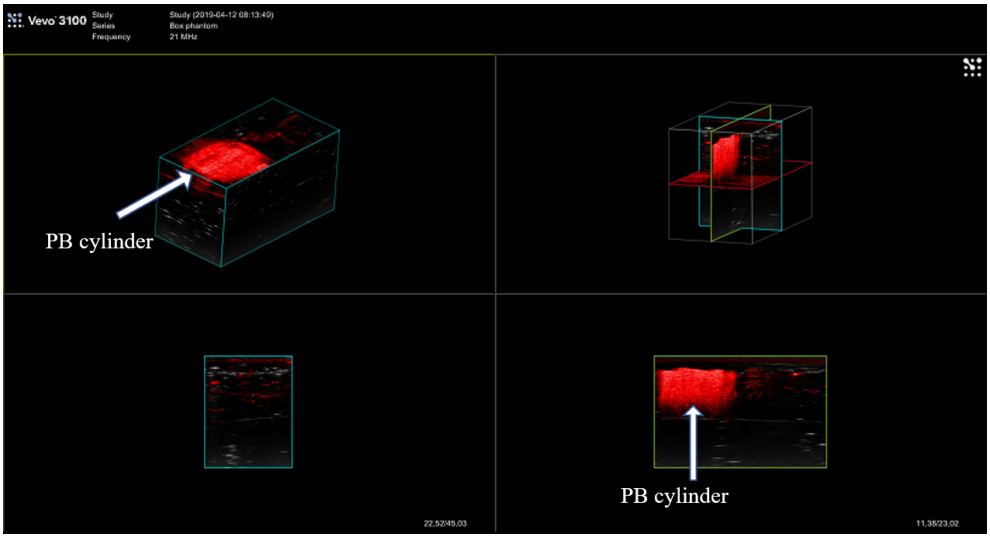

(b)

Figure 4.41: Scanning photoacoustic images of the box phantom at (a) 680 nm: (b) 850 nm.

The upper left image is the 3D reconstruction of the space scanning which can be moved at any direction and illustrating the round shape of the cross section. The bottom-right image is the image of the incident surface of the phantom. It can be seen from the two figures that the shape of the cylindrical inclusion was easily detected. In terms of the visibility of the cylindrical inclusion, the PB inclusion was visible at both two wavelength while the LG inclusion could be seen only at 680 nm. This corresponds to the result when testing the slab phantom and the ink-turpentine absorption spectrum. It also means that the colored ink can be distinguished by the PAI system.

Chapter 5

Conclusion and outlook

In this thesis project, development and characterization of tissue-mimicking phantom materials are studied. Materials for normal liquid and water-based phantoms were summarized and discussed. The optical properties of India ink and Intralipid, as the most widely used absorber and scatterer, were characterized. Three brands of India ink were measured by CTS and the results were similar with typical reference values. The scattering property of Intralipid was measured by the same method and a good coincidence was found with a classical fitting formula presented in other work. Liquid phantoms made with deionized water, India ink base and Intralipid were produced to test the pToFS system. The fitting result indicated that the scattering effects of India ink may bot be neglected. It also showed that the white MC fitting program in the pToFS system may need to be improved.

Materials for solid phantoms, especially oil-based solid phantoms that can be used for PAI were studied. A review of literature suggested several potential polymer materials as phantom bases. SEBS material was adopted as background material since it provided similar acoustic properties as those of biological tissues. Special oil-based colored-ink that were usually used for painting were selected as absorbers in the near-infrared region. The absorption properties of three different colored inks were characterized by measuring the bases made of inks dissolved in turpentine. PAI phantoms were manufactured by mixing the colored inks and TiO_2 in SEBS. A layered phantom was made with SEBS of three colors and a clear reference. The photoacoustic images showed that it was capable to testing the depth resolution of the PAI system. A box phantom with three cylindrical colored SEBS inclusions in surrounding scattering SEBS background containing TiO_2, was also produced. Consisting of both absorbers and scatterer, the measured photoacoustic images of the box phantom showed that the colored ink provided different visibility at different wavelength. Images produced by 3D scanning reconstruction proved that the PAI system was able to detect the shape of the inclusions.

However, there are still improvements to be done. An upgrade of the MC fitting program in pToFS could be a future topic. As for the SEBS phantoms, although the acoustic property of SEBS phantoms has been studied in other paper, research of the influence of colored ink-turpentine base on the SEBS material could be carried out. What is more, some other absorbers such as coffee, the absorption properties of which is similar to melanin, could also be of interest to be used in tissue-mimicking phantoms.

Acknowledgements

I hereby want to thank all the people who have helped me during the research of my thesis project.

First, I want to thank my supervisors, Nina Reistad, Magnus Cinthio and Sune Svanberg. Thank you, Nina, for always being a strict teacher who encouraged me to work with passion and independence. You are more like an honest friend to me. I am grateful for the suggestion of starting to write my report early in the beginning and the detailed feedback comments at the end. I would like to thank Magnus, for spending your time on SEBS phantoms and in the PAI laboratory with me. Your help and suggestions were valuable. I would also like to thank Sune Svanberg for caring for the young student, carefully reading and correcting the text, and offering me the chance to visit the research group in South China Normal University, Guangzhou, China.

I also want to thank the people who made my thesis project happen and develop. I want to give my appreciation to Malin Malmsjö from the Department of Ophthalmology, Clinical Sciences Lund, Lund University. There would not be this thesis project and I would not have access to the PAI system without your kind help. I would like to thank Tobias Erlöv, who came up with a lot practical suggestions and helped me a lot operating the PAI system. And my sincere company in the laboratory, Brian Angeli. It was a great experience to work with you. I also want to thank Emilie Krite Svanberg for help in the laboratory.

Finally, I want to thank my family, my dear parents who always encourage me on keep moving forward and support my living. I hope I do live up to your expectations. Thank you all!

Bibliography

[1] L. C. Cabrelli, F. W. Grillo, D. R. T. Sampaio, A. A. O. Carneiro, and T. Z. Pavan. Acoustic and elastic properties of glycerol in oil-based gel phantoms. *Ultrasound in Medicine & Biology*, 43(9):2086 – 2094, 2017.

[2] L. C. Cabrelli, P. I. B. G. B. Pelissari, A. M. Deana, A. A. O. Carneiro, and T. Z. Pavan. Stable phantom materials for ultrasound and optical imaging. *Physics in Medicine and Biology*, 62(2):432–447, 2017.

[3] G. Quarto, A. Pifferi, I. Bargigia, A. Farina, R. Cubeddu, and P. Taroni. Recipes to make organic phantoms for diffusive optical spectroscopy. *Applied Optics*, 52(11):2494–2502, 2013.

[4] V. Tuchin. *Tissue optics: light scattering methods and instruments for medical diagnosis*. SPIE press Bellingham, 2007.

[5] L. G. Henyey and J. L. Greenstein. Diffuse radiation in the galaxy. *Astrophysical Journal*, 93:70–93, 1941.

[6] J. Jönsson and E. Berrocal. Simulation of light scattering and imaging of spray systems using the open-access software "Multi-Scattering". In *Proceedings of the 29th European Conference on Liquid Atomization and Spray Systems (ILASS-Europe 2019), Paris, France*, 2019.

[7] A. Ishimaru. *Wave propagation and scattering in random media*, volume 2. Academic press New York, 1978.

[8] M. S. Patterson, B. Chance, and B. C. Wilson. Time resolved reflectance and transmittance for the noninvasive measurement of tissue optical properties. *Applied optics*, 28(12):2331–2336, 1989.

[9] M. S. Patterson, S. J. Madsen, J. D. Moulton, and B. C. Wilson. Diffusion equation representation of photon migration in tissue. In *1991 IEEE MTT-S International Microwave Symposium Digest*, pages 905–908. IEEE, 1991.

[10] T. J. Farrell, M. S. Patterson, and B. C. Wilson. A diffusion theory model of spatially resolved, steady-state diffuse reflectance for the noninvasive determination of tissue optical properties in vivo. *Medical Physics*, 19(4):879–888, 1992.

[11] A. H. Hielscher, S. L. Jacques, L.H. Wang, and F. K. Tittel. The influence of boundary conditions on the accuracy of diffusion theory in time-resolved reflectance spectroscopy of biological tissues. *Physics in Medicine and Biology*, 40(11):1957–1975, 1995.

[12] I. J. Duderstadt and L. I. Hamilton. *Nuclear reactor analysis*. Wiley, 1976.

[13] L.H. Wang, S. L. Jacques, and L.Q. Zheng. MCML-monte carlo modeling of light transport in multi-layered tissues. *Computer methods and programs in biomedicine*, 47(2):131–146, 1995.

[14] L. Spinelli, M. Botwicz, N. Zolek, M. Kacprzak, D. Milej, P. Sawosz, A. Liebert, U. Weigel, T. Durduran, F. Foschum, A. Kienle, F. Baribeau, S. Leclair, J. P. Bouchard, I. Noiseux, P. Gallant, O. Mermut, A. Farina, A. Pifferi, A. Torricelli, R. Cubeddu, H. C. Ho, M. Mazurenka, H. Wabnitz, K. Klauenberg, O. Bodnar, C. Elster, M. Bénazech-Lavoué, Y. Bérubé-Lauzière, F. Lesage, D. Khoptyar, A. A. Subash, S. Andersson-Engels, P. Di Ninni, F. Martelli, and G. Zaccanti. Determination of reference values for optical properties of liquid phantoms based on intralipid and india ink. *Biomedical Optics Express*, 5(7):2037–2053, 2014.

[15] F. W. Grillo, L. C. Cabrelli, D. R. T. Sampaio, Antonio A. O. Carneiro, and T. Z. Pavan. Glycerol in oil-based phantom with improved performance for photoacoustic imaging. In *2017 IEEE International Ultrasonics Symposium (IUS)*, pages 1–4. IEEE, 2017.

[16] G. Kim, S.W. Huang, K. C. Day, M. O'Donnell, R. R. Agayan, M. A. Day, R. Kopelman, and S. Ashkenazi. Indocyanine-green-embedded pebbles as a contrast agent for photoacoustic imaging. *Journal of biomedical optics*, 12(4):044020, 2007.

[17] A. I. Chen, M. L. Balter, M. I. Chen, D. Gross, S. K. Alam, T. J. Maguire, and M. L. Yarmush. Multilayered tissue mimicking skin and vessel phantoms with tunable mechanical, optical, and acoustic properties. *Medical Physics*, 43(6 Part1):3117–3131, 2016.

[18] P. D. Ninni, F. Martelli, and G. Zaccanti. The use of india ink in tissue-simulating phantoms. *Optics Express*, 18(26):26854–26865, 2010.

[19] B. W. Pogue and M. S. Patterson. Review of tissue simulating phantoms for optical spectroscopy, imaging and dosimetry. *Journal of Biomedical Optics*, 11(4):41102–1–16, 2006.

[20] H. J. V. Staveren, C. J. M. Moes, J. V. Marie, S. A. Prahl, and M. J. C. V. Gemert. Light scattering in lntralipid-10% in the wavelength range of 400–1100 nm. *Applied Optics*, 30(31):4507–4514, 1991.

[21] R. Michels, F. Foschum, and A. Kienle. Optical properties of fat emulsions. *Optics Express*, 16(8):5907–5925, 2008.

[22] J. R. Cook, R. R. Bouchard, and S. Y. Emelianov. Tissue-mimicking phantoms for photoacoustic and ultrasonic imaging. *Biomedical Optics Express*, 2(11):3193–3206, 2011.

[23] S. E. Bohndiek, S. Bodapati, D. Van De Sompel, S. R. R. Kothapalli, and S. S. Gambhir. Development and application of stable phantoms for the evaluation of photoacoustic imaging instruments. *PloS one*, 8(9):e75533, 2013.

[24] E. Maneas, W. Xia, O. Ogunlade, M. Fonseca, D. I. Nikitichev, A. L. David, S. J. West, S. Ourselin, J. C. Hebden, T. Vercauteren, and A. E. Desjardins. Gel wax-based tissue-mimicking phantoms for multispectral photoacoustic imaging. *Biomedical Optics Express*, 9(3):1151–1163, 2018.

[25] Benjamin Meirza. Development of vessel phantoms for ultrasound methods. Master's thesis, Lund University, 2018.

[26] L. C. Cabrelli, P. I. B. G. B. Pelissari, L. P. Aggarwal, A. M. Deana, A. A. O. Carneiro, and T. Z. Pavan. Oil-based gel phantom for ultrasound and optical imaging. In *Biophotonics South America*, volume 9531, page 95310L. International Society for Optics and Photonics, 2015.

[27] L. C. Cabrelli, D. R. T Sampaio, J. H. Uliana, A. A. O. Carneiro, T. Z. Pavan, and A. M. de Ana. Copolymer-in-oil phantoms for photoacoustic imaging. In *2015 IEEE International Ultrasonics Symposium (IUS)*, pages 1–4. IEEE, 2015.

[28] M. Firbank, M. Hiraoka, and D. T. Delpy. Development of a stable and reproducible tissue-equivalent phantom for use in infrared spectroscopy and imaging. *Proc.SPIE*, 1888:264–271, 1993.

[29] T. Svensson, E. Alerstam, D. Khoptyar, J. Johansson, S. Folestad, and S. Andersson-Engels. Near-infrared photon time-of-flight spectroscopy of turbid materials up to 1400 nm. *Review of scientific instruments*, 80(6):063105, 2009.

[30] L. V. Wang and G. Liang. Photoacoustic microscopy and computed tomography: from bench to bedside. *Annual Review of Biomedical Engineering*, 16:155–185, 2014.

[31] R. Sheikh, M. Cinthio, U. Dahlstrand, T. Erlöv, M. Naumovska, B. Hammar, S. Zackrisson, T. Jansson, N. Reistad, and M. Malmsjö. Clinical translation of a novel photoacoustic imaging system for examining the temporal artery. *IEEE Transactions on Ultrasonics, Ferroelectrics, and Frequency Control*, 66(3):472–480, 2019.

[32] P. D. Ninni, F. Martelli, and G. Zaccanti. Intralipid: towards a diffusive reference standard for optical tissue phantoms. *Physics in Medicine and Biology*, 56(2):N21–N28, 2010.

[33] E. Alerstam, S. Andersson-Engels, and T. Svensson. White monte carlo for time-resolved photon migration. *Journal of Biomedical Optics*, 13(4):041304, 2008.